

# Reappraisal of purported ca. 3.7 Ga stromatolites from the Isua Supracrustal Belt (West Greenland) from detailed chemical and structural analysis

Mike J. Zawaski<sup>1\*</sup>, Nigel M. Kelly<sup>1,2</sup>, Omero Felipe Orlandini<sup>1,3</sup>, Claire I.O. Nichols<sup>4</sup>, Abigail C. Allwood<sup>5</sup> and Stephen J. Mojzsis<sup>1,6\*</sup>.

<sup>1</sup>. Department of Geological Sciences, University of Colorado Boulder, 2200 Colorado Avenue, Boulder, CO 80309-0399, USA. [zawaski@colorado.edu](mailto:zawaski@colorado.edu)

<sup>2</sup>. Bruker Nano Analytics, Bruker Nano Analytics, Am Studio 2D, 12489 Berlin, Germany. [Nigel.Kelly@bruker.com](mailto:Nigel.Kelly@bruker.com)

<sup>3</sup>. Department of Geological Sciences, University of Texas at Austin, 2275 Speedway Stop C9000, Austin, TX 78712 – 1722. [omero.orlandini@jsg.utexas.edu](mailto:omero.orlandini@jsg.utexas.edu)

<sup>4</sup>. Department of Earth, Atmospheric, and Planetary Sciences, Massachusetts Institute of Technology, 77 Massachusetts Avenue, Cambridge, MA 02139-4307. [cion2@mit.edu](mailto:cion2@mit.edu)

<sup>5</sup>. NASA Jet Propulsion Laboratory, 4800 Oak Grove Drive, Pasadena, CA 91109. [Abigail.C.Allwood@jpl.nasa.gov](mailto:Abigail.C.Allwood@jpl.nasa.gov)

<sup>6</sup>. Institute for Geological and Geochemical Research, Research Centre for Astronomy and Earth Sciences, Hungarian Academy of Sciences, 45 Budaörsi Street, H-1112 Budapest, Hungary.

\* Corresponding authors: [zawaski@colorado.edu](mailto:zawaski@colorado.edu) and [mojzsis@colorado.edu](mailto:mojzsis@colorado.edu)

Abstract: 283 words

Main Text: 6416 words

Figures: 10

Tables: 0

References: 50

Supplementary Online Information: Figures: 8, Tables: 1.

M. Zawaski ORCID ID. 0000-0002-4235-6510

N.M. Kelly ORCID ID. 0000-0002-0486-8275

O.P. Orlandini ORCID ID. 0000-0002-9578-1203

C.I.O. Nichols ORCID ID. 0000-0003-2947-5694

A.C. Allwood ORCID ID. NA

S.J. Mojzsis ORCID ID. 000-0003-0000-125X

**Highlights.**

- Claimed ca. 3.7 Ga Isua stromatolites are instead granoblastic quartz + dolomite boudins.
- Absence of characteristic internal convex upward laminae precludes classification as a stromatolite.
- 3-D structural analysis reveals the boudins form ridges parallel to regional deformation.
- Parallel micro- and macro-structural and chemical analyses are essential to assess biogenicity of any proposed bio-structures in ancient, deformed terranes.



**Abstract.** The biogenicity of proposed stromatolite structures from Eoarchean (ca. 3.71 Ga) rocks of the Isua Supracrustal Belt (ISB) of West Greenland is under debate. The “structures” in question are found within a suite of multiply deformed greenschist- to amphibolite metamorphic facies rocks. To assess their promise as primary sedimentary structures – as opposed to products of strain localization in layered, ductile rocks – we report new field mapping at the appropriate scale and resolution from the original discovery site of Nutman et al. (2016). Our new map was used to guide micro- and macro-structural investigations and comprehensive geochemical sampling. Here, we report detailed field characterization and structural analysis to show that the structures are linear inverted ridges aligned with azimuths of local and regional fold axes and parallel to linear structures; they are not deformed conical stromatolites. Combined major element (e.g., Ca, Mg, Si) scanning  $\mu$ XRF maps, and electron backscatter diffraction (EBSD) patterns collected on fresh surfaces cut perpendicular and parallel to the ridges attest to the lack of any residual sedimentary laminae (e.g., compositional layering) within these structures’ cores. Internal layering previously inferred for these features instead arises from variable weathering of outcrop surfaces that otherwise conceals granoblastic quartz  $\pm$  dolomite cored boudins that sit between semi-continuous competent layers of enveloping quartzite in a calc-silicate schist. The morphology of boudins reflect viscosity contrasts of the different ductile layers during deformation. Therefore, these features are not of sedimentary origin. Furthermore, discontinuous field relationships preclude confident assignment of these outcrops as being structurally overturned, as originally argued. Collectively, our results show that the Isua structures are the expected result of a tectonic fabric that preserves no fine-scale primary sedimentary structures of what were probably never stromatolites. (283 words)

**Key words**

Isua Supracrustal Belt; stromatolites; Archean; biosignature; deformation; abiotic

## 1. Introduction

The Isua Supracrustal Belt (ISB) in southern West Greenland (**Fig. 1**) comprises one of the best-preserved, oldest suite of rocks of volcanic-sedimentary protoliths documented for the Eoarchean (pre-3.7 Ga). The ISB is part of the ~3000 km<sup>2</sup> Itsaq Gneiss Complex, a terrane which has experienced a multiphase thermal and deformation history during its 3.7-3.85 Gyr crustal residence time (e.g. Nutman et al., 1996). The ISB rocks are heterogeneously strained, variably metamorphosed at upper greenschist to amphibolite facies conditions, and locally extensively metasomatized by H<sub>2</sub>O-, CO<sub>2</sub>-, carbonate- and/or saline-rich fluids (e.g., Nutman et al., 2004; Rollinson, 2002; Rose et al., 1996; Rosing et al., 1996). Although nearly all primary mineralogy of the ISB has been transformed during recrystallization accompanying metamorphism and deformation, rare low-strain domains do exist. For example, in rare cases primary sedimentary and igneous features such as conglomerates, graded bedding and pillow basalt structures are documented within relatively low strain zones (e.g., Komiya et al., 1999; Maruyama et al., 1991).

One such “low strain” zone is a small (~30 × ~70 m) area within the northeastern limb of the ISB that is argued to preserve recognizable primary sedimentary features, including stretched conical and domical biogenic stromatolites within a layered chert + dolomite rock of marine sedimentary origin (Nutman et al., 2016). This controversial interpretation was based on gross morphological (external shape) comparisons with younger stromatolite structures widely interpreted to be biogenic in origin. It should be emphasized that a biogenic origin for stromatolite structures implies the presence of layers (expressed both mineralogically and geochemically) which are formed by microbial communities that trap and bind sediments, or serving as loci for mineral precipitation. If the interpretation of these features reported from the ISB is correct, such microbial sedimentary structures survived the recrystallization, deformation, and pervasive metasomatic alteration events widely documented by the regional geology (Nutman and Friend, 2009). They would represent the oldest morphological evidence for life, approximately 200 Myr older than the previously oldest known examples from Western Australia (Walter et al., 1980; cf. Lowe 1994).

### <Figure 1-1.5-column fitting image >

The main premise for how sedimentary structures like stromatolites could be preserved at the ISB outcrops rests on the argument that they escaped ductile deformation within small-scale (~10 m) strain haloes formed by fold hinges (Nutman et al., 2016). Further, that the abundance of dolomite and the lack of actinolite was used to suggest limited mobility of Fe-poor fluids with H<sub>2</sub>O:CO<sub>2</sub> values that remained uniform. Each of these assertions were challenged in Allwood et al. (2018). Notwithstanding disputes over whether or not the rocks at these particular Isua outcrops preserve actual stromatolite structures, or are the relicts of purely non-biological processes, the debate can be viewed as part of a larger discussion surrounding the assignment of the term “stromatolite” to any such forms found within the oldest geologic records (e.g., Bontognali et al., 2012; Brasier et al., 2006; Buick et al., 1981; Grotzinger and Knoll, 1999; Hofmann, 2000; Ohtomo et al., 2014; Riding, 2011a). For example, some original sedimentary structures such as tufa (porous calcium carbonate rock formed by precipitation from water) or 3-D crystal growths, can share characteristics resembling biogenic stromatolites (e.g., Grotzinger and Knoll, 1999). These abiotic forms can even present biogenetic characteristics such as internal layering and upward dome forms, but lack other indicators such as interstitial debris. Furthermore, even in relatively well preserved younger stromatolites, carbonaceous micro-fossils and organic matrix components that could be targets for *in situ* isotopic analysis are usually rare or absent (e.g., Brasier et al., 2006; Baumgartner et al., 2019). Given these notable caveats, general agreement exists that any

unambiguous conclusion reached about the biogenicity of a purported stromatolite found in the rock record ought to be based on a suite of criteria that include more than just morphology, or the presence of some microfossil evidence found therein.

To support a biogenic origin interpretation, two criteria ought to be satisfied. First, do the structures match the descriptive definition for stromatolites: "...laminated, lithified, sedimentary growth structures that accrete away from a point or limited surface of attachment. They are commonly, but not necessarily, of microbial origin and calcareous composition" (Semikhatov et al., 1979). Second, are they biogenic? Examples of questions about biogenicity include: do they have structures matching known biogenic criteria (Buick et al., 1981; Frantz et al., 2015; Grotzinger and Knoll, 1999; Hofmann, 2000)? Did the rocks form in an environment consistent with biological-mediation? Are the structures original to sediments of known age, or are they a result of some later geologic history?

Here, we present a re-evaluation of the structures presented as biogenic stromatolites in Nutman et al. (2016), and challenged by Allwood et al. (2018). Our work is based on new field characterization, and mineralogical-geochemical analysis of the discovery site of Nutman et al. (2016) and assesses – from the micrometer- to kilometer scale – how the structures fit into the larger deformation and compositional landscape of the ISB. In our analysis we use a multi-part approach to separate the descriptive (e.g., layering, morphology) and historical (e.g., age, metamorphic, and deformation history) aspects from the interpretive component (i.e., biogenicity). A robust interpretation of these features is significant, as a biogenic origin would extend the record of stromatolites well beyond the oldest-known such features from ca. 3.5 Ga rocks of the Pilbara Block of Western Australia (Allwood et al., 2006; Buick et al., 1981; Wacey, 2010). Such a discovery would move the emergence of relatively complex microbial communities solidly within the first ~800 Myr of Earth history (e.g., Mojzsis et al., 1996).

## 2. Analytical and structural field methods

Our first-order aim was to analyze the structures at the appropriate scales necessary to interpret the geology. Detailed field mapping (1:1250 scale; **Fig. 2**) was conducted over two field seasons (2018 and 2019), and the results were used to guide sampling and structural analysis. All features previously identified by Nutman et al. (2016) as stromatolites, and any features similar in appearance, were examined and measured, with detailed photographs taken for documentation. A sampling moratorium imposed by the provincial government of Greenland on the discovery location, *site A* of Nutman et al. (2016), limited our direct collection of new samples to the outcrop periphery where structures matching those described could be found. Archival samples from the center of *site A* documented in both Allwood et al. (2018) and Nutman et al. (2016), were provided to us on loan from Greenland Ministry of Mineral Resources, Labor and the Interior (A. Juul-Nielsen, *personal communication*). Additional samples were collected from within a layer at *site B* (Nutman et al., 2016), suggested to preserve additional stromatolitic structures as these were outside the moratorium zone.

<Figure 2- 2-column fitting image >

### 2.1 Microchemical analysis

The distribution of major and trace elements in slabbed hand specimens from *site A* and *site B* were recorded using a bench-top M4 Tornado  $\mu$ XRF (Bruker Nano Analytics) equipped with dual 30 mm<sup>2</sup> silicon drift detectors at the Department of Geology and Geological Engineering, Colorado

School of Mines. The instrument is equipped with a Rh X-ray tube with polycapillary optics achieving a spot size of ~25  $\mu\text{m}$ . Measurements were made under vacuum (~20 mbar) at 50 kV and 600  $\mu\text{A}$ , with no primary X-ray source filter. Step sizes and dwell times employed for each sample are given in the figure captions. In addition to Isua samples, we chose additional samples for  $\mu\text{XRF}$  mapping as reference morphological analogues to the structures described from *site A* (following the comparison presented in Nutman et al., 2016). These included a stromatolite from the Woolly Dolomite (Bekker et al., 2016) which was metamorphosed to lower greenschist facies conditions (A. Bekker, *personal communication*), and an undeformed stromatolite from the Early Triassic, Virgin Limestone Member (Moenkopi Formation; Pruss and Payne, 2009; Schubert and Bottjer, 1992). We applied the same chemical analyses to these known biogenic reference samples as a proof-of-concept to determine if element mapping may be used to validate layering within a stromatolite. The  $\mu\text{XRF}$  maps from the ISB samples were additionally processed to produce mineral distribution maps using the Bruker AMICS™ automated mineralogy software. False color mineral maps are presented in **Supplementary Figures 1-4**.

## 2.2 Microstructural analysis

To assess if the target structures accumulated (at the mineral scale) equivalent strain to the regional geology (see Sec. 3.1), we performed electron backscatter diffraction (EBSD) analysis using a Hitachi SU3500 Scanning Electron Microscope with an Oxford Instruments Nordlys Nano detector EBSD at the Nanomaterials Characterization Facility of the University of Colorado Boulder on uncoated, oriented polished thin sections. The instrument was operated at an accelerating voltage of 15kV in low-vacuum (10 Pascals). Data from EBSD were used to quantify the shape preferred orientation (SPO) and crystallographic preferred orientation (CPO) of grains relative to regional structures. The SPO is calculated using the trend of the long axis of an equal-area ellipse from the method described in Mulchrone and Choudhury (2004). Based upon a typical ~100-200  $\mu\text{m}$  grain size observed by optical microscopy, EBSD data were collected at step sizes calibrated to guarantee a statistically robust minimum of seven measurements per grain.

## 3. Results

### 3.1 Geologic map

The study area (**Fig. 1, 2**) comprises a complex association of layered rocks of both sedimentary and volcanic protolith. Based on previous mapping (Nutman and Friend, 2009), these form part of a regional-scale refolded isoclinal fold. The core of the fold is defined by a basaltic andesite that locally preserves pillow basalt (**Fig. 3a**), with calc-silicate schist and quartzite interlayered with it on meter and centimeter scales. Amphibolite in the southern and northern extents of our map area is inferred to have been juxtaposed along a thrust surface during formation of the regional fold structure (Myers, 2001; Nutman and Friend, 2009). Unit boundaries and compositional layering within units are cut by mafic dikes, taken to be part of the ca. 3.5 Ga Ameralik series (Nutman et al., 2004).

Sedimentary protoliths in the map area are dominantly granoblastic, and locally preserve a compositional layer-parallel foliation ( $S_1$ ) understood to be related to the formation of the regional isoclinal fold (here interpreted locally as  $F_1$ ). Compositional layering and the  $S_1$  foliation have been further re-folded into centimeter to 10s meters scale open to tight upright folds ( $F_2$ ), which have axial planes parallel to the trend of the Ameralik dike (**Fig. 2, 3b, 4a**). Deformation structures within the compositional layering include abundant boudins, as well as pinch and swell features (**Fig. 3c-e**).

The mafic (Ameralik *s.l.*) dikes locally have sheared margins, with country rocks preserving high strain domains close to dike contacts that are characterized by tight to isoclinal folding (e.g., **Fig. 3g**) or transposition of compositional layering and foliations to parallel to the dike margin (e.g., **Fig. 3f**). The sedimentary protoliths may also preserve a weak to moderate axial planar foliation ( $S_2$ ) is defined by biotite, as well as quartz and dolomite. Mineral stretching lineations and the long-axis trend of boudinaged quartz-rich layers and veins are parallel to the axis of  $F_2$  folds (**Fig. 3b-c, 4a**). Structural data collected by us within the mapping area are consistent with published measurements made of folded compositional layering elsewhere in the ISB (e.g., **Fig. 4b**), and to data documented for the eastern portion of Isua (Myers, 2001; Nutman and Friend, 2009). This overall congruency confirms that the structures we investigated in the mapping area in **Figure 2** are the result of regional deformation events and can be interpreted within this context.

<Figure 3- 2-column fitting image >

<Figure 4- 1.5-column fitting image >

### 3.2 Outcrop descriptions

Two ISB outcrops preserve structures put forward by Nutman et al. (2016) as stromatolites. *Site A* (**Fig. 2**) is  $\sim 10\text{ m} \times \sim 2.5\text{ m}$  in area (note white arrows in **Fig. 5**) with the structures in question found in seven traceable layers (**Fig. 5b**). *Site B* (**Fig. 2, Supplementary Figure 5**), constitutes a  $2\text{ m} \times 1\text{ m}$  exposure with the structures found in a single layer. The outcrops at *Sites A and B* are predominantly calc-silicate schist, which is composed of ferroan dolomite with minor and variable quartz, biotite, Fe-oxide, actinolite and calcite. Calc-silicate schist is locally interlayered with continuous to discontinuous layers of quartzite, with or without ferroan dolomite and biotite. For both sites *A and B*, bands richer in dolomite appear more brown on weathered surfaces and white on fresh cuts compared with quartz-rich layers, which appear light brown on weathered surfaces and more blue-gray on fresh exposures. Layering, defined by variations in dolomite and quartz, varies in thickness on centimeter to millimeter scales, with finer-scaled layers showing local evidence for truncation. Evidence for intense deformation can be found within a few meters of the *Site A and B* outcrops (**Fig. 3b, f-i**). Ptygmatic folds of felsic veins are common (**Fig. 5a and Supplementary Figure 5**) and indicate changes to the outcrop's dimensions have occurred; some examples have apparent length reductions of  $\sim 2$ -3.

<Figure 5- 2-column fitting image >

#### 3.2.1 Site A

*Site A* sits in the hinge of an  $\sim 10\text{ m}$   $F_2$  synform (**Fig. 2**). The outcrop features that form the focus on this study are predominantly characterized by generally inverted triangular shapes, which may be slightly rounded, and show a variety of intermediate to irregular shapes. Therefore, to avoid genetic terms the “structures” will henceforth be referred to as “ $\nabla$ -structures” (from the Greek symbol, *nabla*,  $\nabla$ ). In outcrop and hand specimen, and when exposed on fresh surfaces (e.g., the saw-cut shown in **Fig. 5d**), no internal laminae are evident. Cores of  $\nabla$ -structures are quartz-rich ( $\pm$  dolomite, biotite) and have margins that have higher abundances of dolomite and biotite (e.g., **Figure 6**). The  $\nabla$ -structures sit within semi-continuous layers of dolomite-rich calc-silicate schist that preserves variable abundances of biotite and quartz (**Fig. 6**). We documented seventy-five  $\nabla$ -structures from seven different layers in the outcrop (**Fig. 5b**) with three more  $\nabla$ -structures found 6m along strike to the southwest, in an adjacent, deformed exposure (**Fig. 3h**). They range between 0.5 and 4 cm high, and 1.5 to 8 cm wide, and have an average aspect ratio 2. Separation between

∇-structures ranges from 1.5 to  $\geq 37$  cm. Importantly, no consistent pattern in aspect ratio or spacing was detected. For the sixty-one ∇-structures at the main outcrop (white arrows in **Fig. 5**) with a clearly defined triangular shape, nearly all (95%) are asymmetric, with clear relationships to the F<sub>2</sub> fold hinge trace that bisects the outcrop (**Fig. 2, 5**). On the east side of the outcrop (and F<sub>2</sub> axial trace), the majority (94%) have an asymmetry defined by a lean towards the axial trace (west leaning). On the west side, 83% lean toward the axial trace (east leaning). A small (~1 m) zone at the center of the outcrop, in the approximate position of the F<sub>2</sub> fold hinge, preserves a mix of east and west leaning ∇-structures.

### 3.2.2 Site B

*Site B* lies approximately 25 m north of *site A* (**Fig. 2**) and includes a single layer of centimeter tall stromatolites (see Nutman et al., 2016; images presented in **Supplementary Figure 5-7**). The ∇-structures occur as pale-brown globular patches within distinct pinched zones of quartz-rich layers in calc-silicate schist (white arrows in **Supplementary Figure 5b, c**).

### 3.2.3 Three-dimensional structure and orientation of the ∇-structures

When viewed in 3-D, the ∇-structures occur as elongate ridges. This observed morphology is at odds with what was previously described by Nutman et al. (2016) as stretched domal features (**Fig. 7a**), in comports with Allwood et al. (2018) who described the structures as ridges (**Fig. 7b**).

At *site A*, our critical observation is that three of the ∇-structures from the outcrop face re-appear on the back face of the outcrop, with two examples shown in **Fig. 5e-g**. Our analysis shows that the ∇-structures on both sides of the outcrop are from the same layer, that they maintain similar morphologies, dimensions, and separation distances. Significantly, the azimuth of the inferred ridges determined by projecting between outcrop faces (~160°) matches the plunge direction of the other ∇-structures (**Fig. 4a**). The greatest length of a ridge shape was measured where the outcrop thickness is ~34 cm.

Additional observations that help constrain their ridge-shaped-geometry include: 1) dimensions on the outcrop face and the back of the cuts made by previous groups remains constant (Allwood et al., 2018; Nutman et al., 2016); 2) a saw cut parallel to the dominant lineation direction exposes a ∇-structure's apex for 10 cm with no indication of tapering (**Fig. 5d**); 3) in our sample for *site B*, (**Supplementary Figure 5**) that was cut perpendicular to the outcrop, we find that the contact between the ∇-structures and adjacent quartz layers is planar (we would expect that these should taper if the structure was an elongated cone); 4) at *site B*, where calc-silicate schist has weathered recessively, quartz-rich layers preserve ridges in the third dimension (**Supplementary Figure 5b**) that are elongate parallel to F<sub>2</sub> fold axes and mineral stretching lineations (**Fig. 4a**).

Analysis of the planar (i.e., compositional layering) and linear (i.e., the ridge alignment of the ∇-structures, mullions, pinch-and-swell structures, lineations along layers and fold hinges) structural measurements in the mapping area shows a structural coherence consistent with a common deformation history (**Fig. 4a**). Linear features are parallel to the orientation of F<sub>2</sub> hinges and axes, and these features are consistent with structures measured outside the immediate mapping area (**Fig. 4b**). These observations reinforce our conclusion that the structures in the mapping area can be interpreted within the regional deformation context.

### 3.3 Micro-geochemical characterization of ∇-structures

Samples from *Site A* and *Site B* were earmarked for geochemical characterization by  $\mu$ XRF. Sample A1 (presented in Allwood et al., 2018) was collected from close to the center of *Site A* (Location “d” on **Figure 5a**), while sample A2 was collected along strike to the east (Location “c” on **Figure 5a**) where deformation of the layers appears superficially to have been more intense. Element maps collected by  $\mu$ XRF indicate that the quartz-rich cores of the ∇-structures are granoblastic and mineralogically homogeneous. Laminae that may represent recrystallized primary layering are absent (**Figure 6c-d, g-h; Supplementary Figure 1, 2**). This comports with fresh cut surfaces of the ∇-structures (**Figure 6b, f**). On the other hand, the element maps do show continuous to semi-continuous layering in the calc-silicate schist that wraps the quartz-rich ∇-structures. In sample A1, additional 5 mm thick quartz-rich layers above the ∇-structure are present that show evidence for boudinage (pinch and swell with local separation; **Fig. 6c, d**).

Sample B1 (*Site B*; **Supplementary Figure 5**) was collected from the same layer and about 10 cm from the ∇-structures reported from this outcrop by Nutman et al. (2016). These preserve similar pinch and swell features between quartz-rich and dolomite-rich layers as previously documented (**Supplementary Figure 5b-c**). Element maps were collected on surfaces of this sample cut parallel and perpendicular to the outcrop surface (and the orientation of lineations). Observations of fresh cut surfaces with support from element maps on Sample B1a (cut parallel to the outcrop surface) reveal that the domains containing the small ∇-structures are mineralogically and chemically identical and continuous with the dolomite-rich layer above (**Supplementary Figure 5d, e**); both are homogeneous and lack internal laminae. At any rate, element maps of Sample B1b (cut perpendicular to the outcrop surface) show that the contact between the quartz- and dolomite-rich layers is planar, and not undulatory as expected even for a stretched domal stromatolite.

<Figure 6- 2-column fitting image >

<Figure 7- 1-column fitting image >

#### 3.3.1 Reference stromatolite materials: Woolly Dolomite and Virgin Limestone Member (*Moenkopi Formation*)

As a comparison to the ∇-structures observed at Isua,  $\mu$ XRF element maps were collected from cut surfaces of two stromatolite samples of biogenic origin: the ca. 2.0 Ga Woolly Dolomite from Western Australia (**Fig. 8a-c**), and the ca. 250 Ma Virgin Limestone Member of the Moenkopi Formation, Nevada, USA (**Fig. 8d-f**). The Woolly Dolomite stromatolite structure we scanned is 5 cm high, and in hand specimen preserves a clear morphology defined by convex upward laminae (**Fig. 8a**). Element maps emphasize that laminae are defined by spaced Si-rich layers (probably chert; **Fig. 8b**) within dolomite and ferroan dolomite (**Fig 8c**). The element maps show that silica has likely been mobilized along the boundaries of the structure, but the laminated morphology is clearly preserved. The Virgin Limestone shows some post-deposition disruption to the stromatolite structures, but is still dominated by convex-upward laminae of its carbonate matrix (**Fig. 8d**). The Virgin Limestone stromatolite is predominantly calcite and dolomite (**Fig. 8e**), with more finely laminated Si-rich layers that accentuate the convex-upward structures (**Fig. 8f**). Additional element maps are provided in **Supplementary Figures 3 and 4**.

<Figure 8- 2-column fitting image >

### 3.4 EBSD of *Site A* ∇-structures

To better understand the expression of the deformation history throughout the *Site A* outcrop, samples A1 and A2 (**Fig. 5c, d** and **Fig. 5**) were set aside for EBSD analysis. For each sample, polished thin sections were made parallel and perpendicular to the targeted ∇-structure. Some EBSD-derived statistics that arise from this work include: 1) All samples have M-index values near 0.01. M-index is a generic measure of fabric orientation strength (Skemer et al., 2005) where a value of 1 is a single crystal and 0 represents purely random orientations. 2) Grain orientation spread (GOS) of about 0.4° and 0.8° for quartz and dolomite, respectively. GOS is the mean number of degrees each measurement inside of a grain is misoriented from the grain's mean orientation. 3) The pattern aspect ratio was ~1.44 for all quartz and dolomite grains. **Figure 9** shows the grain long-axis orientations for the cuts made perpendicular to the ∇-structures where S<sub>2</sub> fabric would be most obvious. **Supplementary Figure 8 and Table 1** summarize the relevant EBSD-derived statistics. It is important to note that the rose diagrams for both the quartz and dolomite grains share a similar orientation to measured outcrop and hand sample scale foliation (strike and dip of 2°, 69°SE) (**Fig. 6b, 9**).

<Figure 9- 1-column fitting image >

## 4. Discussion

### 4.1 Do the ∇-structures fit the classification as either a primary sedimentary feature or biogenic stromatolite?

To better interpret the ∇-structures, especially given the intensity of deformation, metamorphism, and metasomatism affecting the rocks, we considered possible formation scenarios for the Isua ∇-structures and evaluated working hypotheses that these are preserved primary sedimentary features, or were formed during deformation.

It may be possible that the ∇-structures formed as primary sedimentary structures that include mud cracks or ripples. While mud cracks may have a triangular geometry in cross section they are uncommon in carbonate rocks. They typically form in subaqueous environments where periods of subaerial exposure, and development of mud cracks, are unlikely. With respect to ripple marks, internal laminae (regardless of the composition of the sand-sized particles) and regular spacing between layers is expected, neither of which we see in the quartz-rich ∇-structures at *site A or B*. In addition to stromatolites and leiolites, other microbial (sedimentary) structures that can be considered are those formed on an original sedimentary structure like a ripple (e.g., sand-cored stromatolites; Andrews and Trewin, 2014). Because the original contribution by Nutman et al. (2016, their Figure 1c) used a stromatolite from the ca. 2.03 Ga Woolly Dolomite (Western Australia) as a morphological reference to interpret the ∇-structures, we will evaluate the validity of that comparison, and assessments to other potential biogenic origins for these features.

The Woolly Dolomite stromatolites are well-documented and occur as conical shaped (locally triangular in cross section) structures composed of laminated dolomite and quartz. Beyond their antiquity, it is their morphology that provides an ideal comparison to interpret other ancient stromatolite-like structures. A small number of the ∇-structures from Isua are superficially similar in shape, including asymmetries that – in the Woolly Dolomite – have been attributed to soft-sediment deformation after stromatolite formation (Krapež et al., 2015). Given the actual documented range of ∇-structure shapes, however, which may be attributed to varying degrees of



overprinting deformation, we must look to less equivocal evidence that is not so prone to modification.

The expected internal structure of a biogenic stromatolite, regardless of whether they have a history of metamorphic recrystallization, should be characterized by compositional layering from growth by trapping and binding of sediment. Comparative compositional maps of reference *bona fide* stromatolites (our Woolly Dolomite and Virgin Limestone reference materials) collected using  $\mu$ XRF, unambiguously reveal preservation of internal laminae. These include well-defined convex upward dolomite and quartz laminae, which are thicker on the crest than at the edges (**Fig. 8**). Despite some post-deposition modification, such as diagenesis (e.g., transformation of calcite into dolomite and ferroan dolomite in the Virginia Limestone and Woolly Dolomite, respectively), mobilization of silica along layers and the outermost boundary of the stromatolite structures (prominent in the Woolly Dolomite), and minor dislocation along fractures (Virginia Limestone), the clear mineralogical pattern that results from biogenic growth has been preserved. This is in stark contrast to the Isua  $\nabla$ -structures studied in detail here, which are predominantly defined by granoblastic quartz.

In companion publications, Nutman et al. (2016, 2019) argue that the  $\nabla$ -structures contain internal, convex upward laminae. Yet, this is an interpretation made from a photograph of a weathered outcrop face (*Site A*) and backscattered electron images made across one  $\nabla$ -structure's periphery that contains a gradation in quartz and dolomite abundance. Here, we describe mineralogical and geochemical data for two complete  $\nabla$ -structures from *site A*, which demonstrate that this "layering" appears entirely restricted to and parallel with the margins of the structures. This leads to an apparent concentric zoning, from a broad quartz-rich core to a rind that contains a higher abundance of dolomite, with or without biotite that extends beyond the  $\nabla$ -structures. At *site B*, Nutman et al. (2016) argue for the presence of additional stromatolitic structures, which in this case are globular features composed of ferroan dolomite, with or without a quartz and biotite (i.e. calc-silicate schist) component. They occur in pinched zones of the bounding quartzite layer that is structurally below the dolomite. Element maps of samples from this site (**Supplementary Figure 5**) reveal that no compositional difference exists between these globular features and the carbonate layers structurally above, and conspicuously lack any distinct layering (see the dolomite-rich portion at the top of the sample in **Supplementary Figure 5d-e**).

Our interpretation from element maps, which are less subjective than the interpretation of weathered outcrop surfaces, is that most, if not all  $\nabla$ -structures are absent of internal laminae. While leiolites are also structureless, these are only found in Phanerozoic rocks, and occur as domes (~1 m in diameter) mixed within large domal stromatolites (Riding, 2000). Further, it may be argued that laminae may be lost due to syn-metamorphic recrystallization (Nutman et al., 2019). However, this would require significant metasomatism (exchange of chemical constituents, not just in situ readjustment of grain boundaries) to drive a loss of carbonate and enrichment in silica. Yet, this is at odds with the argument that absence of tremolite militates against such pervasive metasomatism (Nutman et al., 2016). Moreover, the  $\nabla$ -structures are draped by calc-silicate schist that *does* preserve laminae (**Fig. 6**). We conclude that the absence of laminae in the  $\nabla$ -structures relates to an original rock that was mineralogically homogeneous, and fails to match any descriptive stromatolite morphology (Awramik and Grey, 2005; Kalkowsky, 1908; Krumbein, 1983; Monty, 1977; Riding, 2007; Semikhatov et al., 1979). This leads us to conclude that a biogenic origin for the  $\nabla$ -structures at Isua is highly improbable.

## 4.2 Deformation setting of the $\nabla$ -structures at Isua

Given the lack of internal laminae preserved in the  $\nabla$ -structures, we must turn to another explanation for these forms. Nutman et al. (2016) emphasized in their work that only one small area within the *Site A* outcrop was sufficiently preserved from overprinting deformation to retain what they interpret to be stromatolites with internal laminae. It was further argued that any remaining  $\nabla$ -structures in the area are either too deformed, mineralogically altered, or both to the point where assessing them for their biogenicity is unproductive. We have shown that the rocks in this narrow area of low-strain in the “core” of *site A* preserve a similar level of strain to the rocks on the margins, and that a deformation origin is more likely.

To argue our point, we need to first better understand the deformation history and distribution of strain. Our geologic map (**Fig. 2**) reveals the local complex structural history of the Isua rocks and provides a sense of the challenges of interpreting the orientation, lateral continuity within units and contacts between lithologic units, and recognition of primary (sedimentary) features that would be required to assess the origin of the  $\nabla$ -structures. The mapping area, as with much of the northeastern section of Isua, has undergone at least two deformation events:  $D_1$  resulted in the generation of a large-scale  $F_1$  isoclinal sheath fold (Myers, 2001; Nutman and Friend, 2009), and  $D_2$  led to upright folding of  $D_1$  structures to produce open to tight  $F_2$  folds and foliation (**Fig. 2** and **6**, respectively). We conclude that  $D_1$  and  $D_2$  were separate events because the Ameralik dikes preserve sheared margins, are oriented parallel to  $F_2$  axial planes, and cross-cut compositional layering and the layer-parallel  $S_1$  foliation. Also, high- $D_2$  strain domains in the immediately adjacent country rock reflect strain accommodation by rocks in contact with the more rigid dikes during  $D_2$  (**Fig. 3f-g**). Mineral and stretching lineations, and the ridges of pinch and swell structures throughout all outcrops in the map area are parallel to  $F_2$  fold axes (**Fig 4a**), which means that stretching (and so widespread boudinage) either occurred during  $D_2$ , or it occurred during  $D_1$  but that  $D_2$  was co-axial.

An essential component to the biogenicity argument was that while the  $\nabla$ -structures appear as inverted triangles, *site A* and *B* occur on the overturned limb of the large-scale  $F_1$  fold. This argument was based on interpretation of truncated layering in deformed calc-silicate rocks. We argue, however, that based on the documented strain the only conclusive, primary structures indicative of stratigraphic orientation in the map area are well-preserved pillow basalts (**Fig. 3a**). Problematically, this volcanic rock layer and adjacent boundary with overlying calc-silicate rocks cannot be traced to either *site A* or *B*, and regular and repeated tight folding occurs throughout the area (**Fig. 6b**). We are therefore forced to conclude that the orientation of any feature, not directly in contact with the pillows is ambiguous, and the designation of the  $\nabla$ -structures being located on an overturned limb of the  $F_1$  fold is unsubstantiated.

Next it is critical to understand better the distribution of strain within the map area, particularly between areas of low- and high-strain. At the outcrop scale, for example, quartz-rich  $\nabla$ -structures with well-defined triangular cross-sections similar to the “ideal” example presented by Nutman et al. (2016) (**Fig. 5k**), are preserved across the entirety of *site A*, including the proposed “low-strain” domain (e.g., **Fig. 5a, h, j-k**), and within more obviously deformed rocks proximal to the margin of the Amerilik dike (**Fig. 5a, c**). As we pointed out above, none of these structures share a morphology with documented stromatolites. In addition, within the apparent “low strain” domain, dismembered quartzite layers are present, some preserving mullion and boudin morphologies (e.g., **Fig. 5h-k**). These features are common across the mapping area, including in domains previously characterized as having experienced high degrees of strain (e.g., **Fig. 3c-e**).

To quantitatively evaluate strain distribution, we compare SPO and CPO data collected using EBSD from samples in the “low strain lacuna” at *site A* as described by Nutman et al. (2016), and from an apparently higher strain domain (samples A1 and A2, respectively; **Fig. 5a, c, d**). These data show similar SPOs, grain aspect ratio, M-index, and GOS, all of which suggest both samples currently preserve evidence for a similar level of deformation (**Fig. 9; Supplemental Figure 8; Table 1**). Also, the indicators of strain in these samples correlate most clearly with D<sub>2</sub> compression, consistent with orientations of axial planar S<sub>2</sub> foliations preserved in some areas (e.g., **Fig. 6b**). This points to a similar degree of deformation and recrystallization during the D<sub>2</sub> event. While assignment of “low” versus “high strain” can be subjective (see Marques et al., 2008 and references within), we can now say the ∇-structures across *site A* occur (or formed) within zone of similar deformation intensity and can therefore be equally assessed for their biogenicity.

A final observation is that where recessive weathering of calc-silicate schist exposed multiple surfaces of the quartz-rich ∇-structures (e.g., **Fig 5c**) or trends could be established by projection through an outcrop (e.g., **Fig. 5e-g**), the trends of the ∇-structure ridge axes are seen to be parallel to F<sub>2</sub> fold axes and lineations (**Fig. 4a**). They are also parallel to the trend of ridges formed on quartz-rich layers that show pinch and swell features (e.g., **Fig. 3c, Supplemental Figure 5b**).

Taken together, observations show that they are not deformed cones; they do not present as elongate tapering humps because of volume conservation. Instead they occur as ridges with crests aligned with lineations and F<sub>2</sub> fold axes (**Fig. 7**).

While it is true that ridge-shaped stromatolites are supported from the rock record (Andres and Reid, 2006; Chaudhuri, 1970; Suosaari et al., 2016; Tosti and Riding, 2017; Wacey, 2010), the evidence shows that the ridges at the Isua locality are subparallel to all mapped linear structures, and lack laminae within individual ∇-structures. We regard this as entirely consistent with their origin via boudinage of semi-continuous quartz-rich layers within the calc-silicate schist. This key observation contradicts the idea that the ∇-structures could be a derived form from a pre-tectonic (i.e. originally conical stromatolite) shape that experienced subsequent tectonic deformation(s) (van Loon et al., 2013).

#### 4.3 A deformation model for the Isua ∇-structures

The available evidence from external and internal morphology as ridges, absence of internal mineralogical or geochemical zoning, coupled with the abundant additional evidence for boudinage throughout all outcrops with structural geometries aligning with the ∇-structures leads us to conclude that all the ∇-structures described by Nutman et al. (2016, 2019) are the result of boudinage during deformation. For typical boudin shapes (e.g., lens shaped boudins where pinching occurs equally on upper and lower surfaces of the rheologically more competent layer) the rheology of the host rock is typically considered to be similar above and below the boudin. In the case of the Isua ∇-structures, rounded triangular cross-sections are common, suggesting that the rheology (i.e. competence) of the upper and lower bounding layers was likely not identical and gave rise to the ∇-morphology (e.g., Gardner et al., 2016). While it is outside the scope of this work to evaluate the fine details of a ∇-shaped boudin, the rocks which host the ∇-structures contain mineralogical compositions that match the viscosity contrast needed (quartz > dolomite > biotite) for the ∇-morphology (**Fig. 5, 6, 10**).

The model we favor for the ∇-structures invokes layer-parallel extension of quartz-rich layers within rheologically less competent calc-silicate schist, during either the D<sub>1</sub> or D<sub>2</sub> events (**Fig. 10a-**

c). Differential accommodation of strain, related to strain partitioning and contrasts in composition along and between layers yields a wide variety of related deformation structures, only one of which are the  $\nabla$ -structures described herein. The model also explains the commonly pronounced asymmetry observed in cross-sections of the  $\nabla$ -structures (e.g., **Fig. 5**). Continued deformation during D<sub>2</sub> led to the development of asymmetry, a product of flexural flow along limbs of the prominent F<sub>2</sub> fold that bisects the outcrop area (**Fig. 2; 10d**), consistent with strain models for folds (Cosgrove, 2015; Fossen, 2016; Ramsay, 1967), and is harmonious with the bimodal distribution of asymmetry on either side of the synform at *Site A*.

<Figure 10- 1.5-column fitting image >

## 5. Conclusions

From the descriptive definition of stromatolite, the structures at *site A* and *site B* lack convex upward internal laminae (**Figures 5, 6** and **Supplementary Figure 5**) and thus fail to meet the criteria to be referred to as stromatolites. This point stands regardless of whether the rocks have been overturned. With no internal laminae, it is not possible to classify them as stromatolites and thereby to view them as evidence of ancient life. Returning to our multiple working hypotheses, we argue the  $\nabla$ -structures' origin is best explained as a consequence of the tectonic history of the Isua Supracrustal Belt and it is more coherent that they be referred to as boudins, instead of stromatolites. The evidence supporting a tectonic origin of the  $\nabla$ -structures at *site A* comes from all scales:

1. Our EBSD data supports the notion that all  $\nabla$ -structures within and beyond *sites A & B* have received a similar level of deformation and can then be evaluated equally for biogenicity. There is no requirement that our observations be arbitrarily restricted to “low strain lacunae”.
2. Absence of layering within the structures and a morphology of many of the  $\nabla$ -structures is inconsistent with stromatolites through time and thus refutes their classification as stromatolites (**Fig. 5 c-k**).
3. The morphology of the  $\nabla$ -structures is instead entirely consistent with a tectonic origin, owing to the fact that they: i) are linear (i.e., ridge) shapes oriented parallel to the fold hinges, measured lineations, and  $\pi$ -axis of the planar structures, ii) pinch out on the sides with a  $\nabla$ -morphology, consistent with boudins, and iii) asymmetrically lean inward towards the hinge of the *site A* synform.

To conclude, the best geological interpretation which is coherent with all data is that the  $\nabla$ -structures and the various forms in **Figure 3c-e** (50 m from *sites A and B*) are tectonic fabrics for rocks with variable rheology and competence. We wish to emphasize that categorizing these structures as tectonic does not preclude the possibility that life played some role at some time in the formation of these rocks. That said, evidence for bio-mediation that has been seemingly erased necessitates more assumptions than our pure tectonic scenario. The outcome of our classification places the burden on arguments for biogenicity rather than on abiogenesis.

Debate over assignment of biogenicity (whether as “stromatolite” or some other shape) to such ancient rocks on Earth is fraught with difficulty, despite the fact that they can be interrogated

directly by field geologists on multiple occasions and brought back for laboratory analysis. To first order, we must caution against interpretation of weathered, 2D outcrop surfaces as a means for deducing primary (internal) 3D structure. The entire structure and the material surrounding it must be understood in order to see the complete morphology. These shortcomings reinforce the need for rigorous 3D observations of such structures if they are found to exist, for example, on the ancient surface of Mars. **(6416 words)**

## ACKNOWLEDGMENTS

These ideas contained herein were clarified by discussions and debates with V.R. Bennett, F.A. Corsetti, C.R.L. Friend, J.W. Hagadorn, A. Kappler, S.H. Kopf, A.P. Nutman, M.T. Rosing, and B.A. Wing. This study was supported by the Collaborative for Research in Origins (CRiO) directed by S.J.M. and supported by The John Templeton Foundation (principal investigator: S. Benner/FfAME/Award #54466): the opinions expressed in this publication are those of the authors, and do not necessarily reflect the views of the John Templeton Foundation. S.J.M. also extends a special thanks the University of Lorraine and G. Caro at the CNRS-CRPG (Nancy, France) for a Visiting Professor appointment during significant phases of the preparation of this manuscript. We are grateful to the generous support of the Simons Foundation (Award #556352) to C.I.O.N., and to grant-in-aid awards to M.Z. from the University of Colorado Department of Geological Sciences, and the Colorado Shared Instrumentation in Nanofabrication and Characterization (COSINC) Facility. Permissions for fieldwork and sample collection were granted through the Government of Greenland's Mineral License and Safety Authority. We would also like to thank B. Weiss and A. Eyster (MIT), A. Maloof (Princeton University), and T. Greenfield (University of Cambridge) for their critical assistance in the field. We appreciate A. Juul-Nielsen (Greenland Ministry of Mineral Resources, Labor and the Interior office) for her willingness to loan of essential archival samples from *site A* of Nutman et al., (2016), and to A. Bekker (UC-Riverside) for samples of the Woolly Dolomite.

## REFERENCES CITED

- Allwood, A.C., Rosing, M.T., Flannery, D.T., Hurowitz, J.A., Heirwegh, C.M., 2018. Reassessing evidence of life in 3,700-million-year-old rocks of Greenland. *Nature*. <https://doi.org/10.1038/s41586-018-0610-4>
- Allwood, A.C., Walter, M.R., Kamber, B.S., Marshall, C.P., Burch, I.W., 2006. Stromatolite reef from the Early Archaean era of Australia. *Nature* 441, 714–718. <https://doi.org/10.1038/nature04764>
- Andres, M.S., Reid, R.P., 2006. Growth morphologies of modern marine stromatolites: A case study from Highborne Cay, Bahamas. *Sediment. Geol.* 185, 319–328. <https://doi.org/10.1016/j.sedgeo.2005.12.020>
- Andrews, S.D., Trewin, N.H., 2014. Palaeoenvironmental significance of lacustrine stromatolite forms from the Middle Old Red Sandstone of the Orcadian Basin. *Geol. Mag.* 151, 414–429. <https://doi.org/10.1017/S0016756813000290>
- Awramik, S.M., Grey, K., 2005. Stromatolites: biogenicity, biosignatures, and bioconfusion 5906, 59060P. <https://doi.org/10.1117/12.625556>
- Baumgartner, R.J., Van Kranendonk, M.J., Wacey, D., Fiorentini, M.L., Saunders, M., Caruso, S., Pages, A., Homann, M., Guagliardo, P., 2019. Nano-porous pyrite and organic matter in 3.5-billion-year-old stromatolites record primordial life. *Geology* 47, 1039–1043. <https://doi.org/10.1130/G46365.1>
- Bekker, A., Krapež, B., Müller, S.G., Karhu, J.A., 2016. A short-term, post-Lomagundi positive C isotope excursion at c. 2.03 Ga recorded by the Woolly Dolomite, Western Australia. *J. Geol. Soc. London.* 173, 689–700. <https://doi.org/10.6084/m9.figshare.c.2868055>
- Bontognali, T.R.R., Sessions, A.L., Allwood, A.C., Fischer, W.W., Grotzinger, J.P., Summons, R.E., Eiler, J.M., 2012. Sulfur isotopes of organic matter preserved in 3.45-billion-year-old stromatolites reveal microbial metabolism. *Proc. Natl. Acad. Sci.* 109, 15146–15151. <https://doi.org/10.1073/pnas.1207491109>
- Brasier, M., McLoughlin, N., Green, O., Wacey, D., 2006. A fresh look at the fossil evidence for early Archaean cellular life. *Philos. Trans. R. Soc. B Biol. Sci.* <https://doi.org/10.1098/rstb.2006.1835>
- Buick, R., Dunlop, J.S., Groves, D.I., 1981. Stromatolite recognition in ancient rocks: An appraisal of irregularly laminated structures in an early archaean chert-barite unit from north pole, Western Australia. *Alcheringa* 5, 161–181. <https://doi.org/10.1080/03115518108566999>
- Chaudhuri, A., 1970. PRECAMBRIAN STROMATOLITES IN THE PRANHITA-GODAVARI VALLEY (SOUTH INDIA). *Palaeogeogr. Palaeoclimatol. Palaeoecol.* 7, 309–340.
- Cosgrove, J.W., 2015. The association of folds and fractures and the link between folding, fracturing and fluid flow during the evolution of a fold-thrust belt: a brief review. *Geol. Soc. London, Spec. Publ.* 421, 41–68. <https://doi.org/10.1144/SP421.11>
- Fossen, H., 2016. *Structural Geology*, 2nd ed.
- Frantz, C.M., Petryshyn, V.A., Corsetti, F.A., 2015. Grain trapping by filamentous cyanobacterial and algal mats: implications for stromatolite microfabrics through time. *Geobiology* 13, 409–423. <https://doi.org/10.1111/gbi.12145>
- Gardner, R.L., Piazzolo, S., Daczko, N.R., 2016. Shape of pinch and swell structures as a viscosity indicator: Application to lower crustal polyphase rocks. *J. Struct. Geol.* 88, 32–45.

- <https://doi.org/10.1016/J.JSG.2016.04.012>
- Grotzinger, J.P., Knoll, A.H., 1999. Stromatolites in Precambrian carbonates: evolutionary mileposts or environmental dipsticks? *Annu. Rev. Earth Planet. Sci.* 27, 313–358. <https://doi.org/10.1146/annurev.earth.27.1.313>
- Hofmann, H.J., 2000. Archean Stromatolites as Microbial Archives, in: Riding, R.E., Awramik, S.M. (Ed.), *Microbial Sediments*. Springer, Berlin, pp. 315–327. [https://doi.org/https://doi.org/10.1007/978-3-662-04036-2\\_34](https://doi.org/https://doi.org/10.1007/978-3-662-04036-2_34)
- Kalkowsky, E., 1908. Oolith und Stromatolith im norddeutschen Buntsandstein. *Zeitschrift der Dtsch. Geol. Gesellschaft* 68–125.
- Komiya, T., Maruyama, S., Masuda, T., Nohda, S., Hayashi, M., Okamoto, K., 1999. Plate tectonics at 3.8–3.7 Ga: Field evidence from the Isua Accretionary Complex, southern West Greenland. *J. Geol.* 107, 515–554. <https://doi.org/10.1086/314371>
- Krapež, B., Müller, S.G., Bekker, A., 2015. Stratigraphy of the Late Palaeoproterozoic (~2.03 Ga) Woolly Dolomite, Ashburton Province, Western Australia: A carbonate platform developed in a failed rift basin. *Precambrian Res.* 271, 1–19. <https://doi.org/10.1016/J.PRECAMRES.2015.09.022>
- Krumbein, W.E., 1983. Stromatolites - the challenge of a term in space and time. *Precambrian Res.* 20, 493–531. [https://doi.org/10.1016/0301-9268\(83\)90087-6](https://doi.org/10.1016/0301-9268(83)90087-6)
- Lowe, D., 1994. Abiological origin of described stromatolites older than 3.2 Ga. *Geology* 22, 387–390. [https://doi.org/10.1130/0091-7613\(1994\)022<0387:AODSO>2.3.CO;2](https://doi.org/10.1130/0091-7613(1994)022<0387:AODSO>2.3.CO;2)
- Marques, F.O., Guerreiro, S.M., Fernandes, A.R., 2008. Sheath fold development with viscosity contrast: Analogue experiments in bulk simple shear. *J. Struct. Geol.* 30, 1348–1353. <https://doi.org/10.1016/J.JSG.2008.07.001>
- Maruyama, S., Masuda, S., Appel, P.W.U., 1991. The oldest accretionary complex on the Earth, Isua, Greenland. *Geol. Soc. Am.* 23, A429–A430.
- Mojzsis, S.J., Arrhenius, G., McKeegan, K.D., Harrison, T.M., Nutman, A.P., 1996. Evidence for life on Earth before 3,800 million years ago. *Nature* 384, 55–59.
- Monty, C., 1977. Evolving Concepts on the Nature and the Ecological Significance of Stromatolites, in: *Fossil Algae*. Springer Berlin Heidelberg, pp. 15–35. [https://doi.org/10.1007/978-3-642-66516-5\\_2](https://doi.org/10.1007/978-3-642-66516-5_2)
- Mulchrone, K.F., Choudhury, K.R., 2004. Fitting an ellipse to an arbitrary shape: Implications for strain analysis. *J. Struct. Geol.* 26, 143–153. [https://doi.org/10.1016/S0191-8141\(03\)00093-2](https://doi.org/10.1016/S0191-8141(03)00093-2)
- Myers, J.S., 2001. Protoliths of the 3.8–3.7 Ga Isua greenstone belt, West Greenland. *Precambrian Res.* 105, 129–141. [https://doi.org/10.1016/S0301-9268\(00\)00108-X](https://doi.org/10.1016/S0301-9268(00)00108-X)
- Nutman, A.P., Bennett, V.C., Friend, C.R.L., Van Kranendonk, M.J., Chivas, A.R., 2016. Rapid emergence of life shown by discovery of 3,700-million-year-old microbial structures. *Nature* 537, 535–538. <https://doi.org/10.1038/nature19355>
- Nutman, A.P., Bennett, V.C., Friend, C.R.L., Van Kranendonk, M.J., Rothacker, L., Chivas, A.R., 2019. Cross-examining Earth’s oldest stromatolites: Seeing through the effects of heterogeneous deformation, metamorphism and metasomatism affecting Isua (Greenland) ~3700 Ma sedimentary rocks. *Precambrian Res.* 331, 105347. <https://doi.org/10.1016/J.PRECAMRES.2019.105347>
- Nutman, A.P., Friend, C.R.L., 2009. New 1:20,000 scale geological maps, synthesis and history of investigation of the Isua supracrustal belt and adjacent orthogneisses, southern West

- Greenland: A glimpse of Eoarchaeon crust formation and orogeny. *Precambrian Res.* 172, 189–211. <https://doi.org/10.1016/j.precamres.2009.03.017>
- Nutman, Allen P., Friend, C.R.L., Barker, S.L.L., McGregor, V.R., 2004. Inventory and assessment of Palaeoarchaeon gneiss terrains and detrital zircons in southern West Greenland. *Precambrian Res.* 135, 281–314. <https://doi.org/10.1016/j.precamres.2004.09.002>
- Nutman, Allan P., Friend, C.R.L., Bennett, V.C., McGregor, V.R., 2004. Dating of the Ameralik dyke swarms of the Nuuk district, southern West Greenland; Mafic intrusion events starting from c. 3510 Ma. *J. Geol. Soc. London.* 161, 421–430. <https://doi.org/10.1144/0016-764903-043>
- Ohtomo, Y., Kakegawa, T., Ishida, A., Nagase, T., Rosing, M.T., 2014. Evidence for biogenic graphite in early archaeon isua metasedimentary rocks. *Nat. Geosci.* 7, 25–28. <https://doi.org/10.1038/ngeo2025>
- Pruss, S.B., Payne, J.L., 2009. EARLY TRIASSIC MICROBIAL SPHEROIDS IN THE VIRGIN LIMESTONE MEMBER OF THE MOENKOPI FORMATION, NEVADA, USA. *Palaios* 24, 131–136. <https://doi.org/10.2110/palo.2007.p07-094r>
- Ramsay, G.J., 1967. *Folding and Fracturing of Rocks*. Mc Graw Hill Book Company.
- Riding, R., 2011. The nature of stromatolites: 3,500 million years of history and a century of research, in: *Lecture Notes in Earth Sciences*. pp. 29–74. [https://doi.org/10.1007/978-3-642-10415-2\\_3](https://doi.org/10.1007/978-3-642-10415-2_3)
- Riding, R., 2007. The term stromatolite: towards an essential definition. *Lethaia* 32, 321–330. <https://doi.org/10.1111/j.1502-3931.1999.tb00550.x>
- Riding, R., 2000. Microbial carbonates : the geological record of calcified bacterial and algal mats and biofilms. *Sedimentology* 47, 179–214. <https://doi.org/10.1046/j.1365-3091.2000.00003.x>
- Rollinson, H., 2002. The metamorphic history of the Isua Greenstone Belt, West Greenland. *Geol. Soc. London, Spec. Publ.* 199, 329–350. <https://doi.org/10.1144/GSL.SP.2002.199.01.16>
- Rose, N.M., Rosing, M.T., Bridgwater, D., 1996. The origin of metacarbonate rocks in the archaeon Isua supracrustal belt, west Greenland. *Am. J. Sci.* 296, 1004–1044. <https://doi.org/10.2475/ajs.296.9.1004>
- Rosing, M.T., Rose, N.M., Bridgwater, D., Thomsen, H.S., 1996. Earliest part of Earth's stratigraphic record: A reappraisal of the >3.7 Ga Isua (Greenland) supracrustal sequence. *Geology* 24, 43. [https://doi.org/10.1130/0091-7613\(1996\)024<0043:EPOESS>2.3.CO;2](https://doi.org/10.1130/0091-7613(1996)024<0043:EPOESS>2.3.CO;2)
- Schubert, J.K., Bottjer, D.J., 1992. Early Triassic stromatolites as post-mass extinction disaster forms. *Geology* 20, 883–886. [https://doi.org/10.1130/0091-7613\(1992\)020<0883:ETSAPM>2.3.CO;2](https://doi.org/10.1130/0091-7613(1992)020<0883:ETSAPM>2.3.CO;2)
- Semikhatov, M.A., Gebelein, C.D., Cloud, P., Awramik, S.M., Benmore, W.C., 1979. Stromatolite Morphogenesis - Progress and Problems. *Can J Earth Sci* 16, 992–1015. <https://doi.org/10.1139/e79-088>
- Skemer, P., Katayama, I., Jiang, Z., Karato, S.I., 2005. The misorientation index: Development of a new method for calculating the strength of lattice-preferred orientation. *Tectonophysics* 411, 157–167. <https://doi.org/10.1016/j.tecto.2005.08.023>
- Suosaari, E.P., Reid, R.P., Playford, P.E., Foster, J.S., Stolz, J.F., Casaburi, G., Hagan, P.D., Chirayath, V., Macintyre, I.G., Planavsky, N.J., Eberli, G.P., 2016. New multi-scale



perspectives on the stromatolites of Shark Bay, Western Australia. *Sci. Rep.* 6, 20557.  
<https://doi.org/10.1038/srep20557>  
 Tosti, F., Riding, R., 2017. Fine-grained agglutinated elongate columnar stromatolites: Tieling  
 Formation, ca 1420 Ma, North China. *Sedimentology* 64, 871–902.  
<https://doi.org/10.1111/sed.12336>  
 van Loon, A.J. (Tom), Dechen, S., Yuan, W., Min, L., 2013. Deformed stromatolites in marbles  
 of the Mesoproterozoic Wumishan Formation as evidence for synsedimentary seismic  
 activity. *J. Palaeogeogr.* 2, 390–401. <https://doi.org/10.3724/SP.J.1261.2013.00038>  
 Wacey, D., 2010. Stromatolites in the ~3400 Ma Strelley Pool Formation, Western Australia:  
 Examining Biogenicity from the Macro- to the Nano-Scale. *Astrobiology* 10, 381–395.  
<https://doi.org/10.1089/ast.2009.0423>  
 Walter, M.R., Buick, R., Dunlop, J.S.R., 1980. Stromatolites 3,400–3,500 Myr old from the  
 North Pole area, Western Australia. *Nature* 284, 443–445.  
<https://doi.org/10.1038/284443a0>.

742

## FIGURE CAPTIONS

743 Fig. 1. (a) Greenland and the location of the Isua Supracrustal Belt (ISB). (b) The ISB (green) and  
 744 the location of the study area in West Greenland. The ISB is surrounded by ca. 3.0 Ga tonalitic  
 745 gneisses (light grey) to the north, and the ca. 3.7-3.8 Ga Itsaq Gneiss (dark grey) in the south. The  
 746 ISB wraps around ca. 3.7 Ga granitic and tonalitic gneisses (yellow area in the center of the map).  
 747 Figure modified from Myers, 2001.

748 Fig. 2. Geological map of the area surrounding the proposed stromatolites from Nutman et al.,  
 749 (2016). Stromatolites (A, B), and tempestite (C). The location of preserved pillow basalt (P) is  
 750 also indicated.

751 Fig. 3. Field photographs of structures from the mapping area. The scale bar divisions are in  
 752 centimeters. (a) Pillow structures in basaltic-andesite (“P” in **Fig. 2**). Arrows approximately mark  
 753 pinching of the lower surface of the pillows giving way-up criteria. Pencils for scale. (b) Tight  
 754 folds in interlayered calc-silicate schist and quartzite (outcrop ~20 m north of *site B*; pencil for  
 755 scale). (c) Exposed dip-slope of a quartzite layer, showing a ridge-like morphology on the upper  
 756 surface. The layer below is calc-silicate and biotite-rich schist. The orientation of ridge crests is  
 757 parallel to  $\nabla$ -structures in the *site A* outcrop, and to fold hinges and lineations (e.g., **Fig. 4**). (d)  
 758 Boudins of a quartz-rich layer in calc-silicate schist. The calc-silicate matrix is showing evidence  
 759 for ductile flow into boudin necks in a zone of higher relative deformation. (e) Pinch-and-swell  
 760 structures within interlayered quartzite and calc-silicate schist. (f) Photograph (looking south) of  
 761 an outcrop at the north end of the map area illustrating 10 meter-scale folding of compositional  
 762 layering (and layer-parallel  $S_1$  gneissosity) in quartzite adjacent to the post- $D_1$  and pre- or syn- $D_2$   
 763 Ameralik dike. The axis to this fold is co-linear with other  $F_2$  fold axes and  $L_2$  lineations. See the  
 764 geologic map for fold extent (**Fig. 2**) (40 cm hammer for scale). (g) Calc-silicate schist preserving  
 765 high strain (dotted line outlining folding) in contact with Ameralik dike (dashed line, 18.5 cm tall  
 766 notebook for scale). (h)  $\nabla$ -structures, 6m along strike in the same layer as *site A*, within calc-  
 767 silicate schist containing tightly folded layering. Quartz-rich layers are weathering prominently.  
 768 (i) Centimeter to decimeter-scale folding of layered calc-silicate schist containing local quartzite  
 769 and quartz-rich schist layers (~10 m south of *site A*; ~8 cm wide compass for scale).

770 Fig. 4. (a) Equal-area stereonet for structural data collected in the map area (**Fig. 2**) showing trends  
 771 of compositional layering (black circles are poles to layering,  $n=139$ ) and linear structures (fold  
 772 hinges ( $n=23$ ), blue squares; lineations ( $n=45$ ), black triangles; and  $\nabla$ -structures ( $n=7$ ), red and  
 773 orange diamonds. The  $\pi$ -axis, the pole to the best fit girdle through the poles to compositional  
 774 layering (red square), is also given. (b) Stereonet for measurements of compositional layering  
 775 taken from ISB locations outside the map area ( $n=12$ ). Note that data define a fold identical in  
 776 orientation as folds in the map area.

777 Fig. 5. Field photographs taken of outcrops corresponding to *Site A* from Nutman et al., (2016)  
 778 and Allwood et al., (2018). Scale bar is 1 cm unless otherwise noted. All images (and therefore  
 779  $\nabla$ -structures (white arrows) and other features) are oriented as seen in outcrop. (a) Photograph of  
 780 the fully exposed outcrop at Site A. Arrows indicate the location of photographs in **Figures 5b-k**.  
 781 (b) Same photograph as in (a), but with layers hosting ridge structures indicated. These are  
 782 numbered and references as L1-L7 in the text. (c) Weathered  $\nabla$ -structure from layer 4, sampled  
 783 for analysis (Sample A2 from *site A* east side). (d) A saw-cut made by Allwood et al. (2018) in  
 784 Layer 4. The cut, which is perpendicular to the outcrop face, exposes an apparently thick quartz-

rich layer that is the result of the cut being aligned along the apex of the ridge-shaped  $\nabla$ -structure. The uniform thickness of the layer within the exposed surface is evidence that the  $\nabla$ -structures are ridges (the cut is 10 cm deep) and not stretched cones. Sample A1 from *site A* west side was taken from this saw cut. (e, f, g) Front, back and side views, respectively, of the outcrop exposing two structures (labeled 1 and 2) from Layer 4. The  $\nabla$ -structures are interpreted to extend from front to back of the outcrop along a trend parallel to location lineations and fold hinges. In addition, both  $\nabla$ -structures are similar in morphology, dimensions, and separation. The outcrop is ~17 cm thick at this location. (h) Three  $\nabla$ -structures from Layer 3. Note the effect of differential weathering - the quartz-rich cores of the two  $\nabla$ -structures to the right have weathered less than the carbonate- and mica-rich layers. The lower portion of the outcrop has weathered at an oblique angle to the vertical face, which increases the apparent thickness of the outer portion of the structures. Note the pinch and swell features in the quartz-rich layers at the top of the image. (i) Pinch and swell features in quartz-rich layers of Layer 4. The left-most layer fragment resembles a mullion. (j) A  $\nabla$ -structure ~ 20 cm below the  $\nabla$ -structures (k) originally presented in Nutman et al., (2016). Note that core domains in the  $\nabla$ -structures are homogeneous.

Fig. 6. Outcrop and hand sample images of  $\nabla$ -structures, with corresponding element maps collected by  $\mu$ XRF. Scale bar is 1 cm for all images. (a-d) Sample A1, from the center of *Site A* (west side), Layer 4. This sample was collected by Allwood et al., (2018). (a) Photograph of the weathered surface of Sample A1 (See **Fig. 5d**). (b) The cut surfaces of the sample. The quartz-rich core of the  $\nabla$ -structure appears gray-blue and the carbonate-rich outer zones appear white. Layering is penetrated by a foliation that cuts layering in the rock (yellow arrows). (c-d) Element maps of sample A1 collected by  $\mu$ XRF with a step size of 25  $\mu$ m and dwell time per pixel of 25 ms. Purple-pink colors in (c) represent presence of both Ca and Mg, in the absence of abundant Si. Orange colors in (d) represent the presence of Ca and Fe. These maps suggest that the quartz-rich core to the  $\nabla$ -structure is enveloped by layering dominated by ferroan dolomite. (e-h) Sample A2, from the east side of *Site A*, Layer 4 (See **Fig. 5c**). (e) Photograph of the sampled  $\nabla$ -structure. (f) Photograph of a cut surface on the same hand sample. (g and h) Element maps of sample A2 collected by  $\mu$ XRF, collected with a step size of 25  $\mu$ m and dwell time per pixel of 35 ms. Element combinations are interpreted to represent similar mineral associations as in Sample A1. In addition, layering in the schist above the quartz-rich  $\nabla$ -structure is locally biotite rich (green domains). The dashed lines in (d) trace the semi-continuous layers around the core.

Fig. 7. Schematic cartoons of two possible morphologies for the  $\nabla$ -structures at *site A*. (a) An elongated cone or dome, which would be the expected shape if an original conical structure existed (e.g., stromatolite) and was stretched during deformation but has conserved the original volume. (b) A ridge-shaped structure that formed due to layer-parallel extension during deformation (boudinage). The blue triangle is the surface expression on the outcrop generated by either  $\nabla$ -structure.

Fig. 8. Examples of biogenic stromatolites from the rock record. Scale bar is 1 cm. (a-c) ca. 2.0 Ga Woolly Dolomite (Western Australia), and (d-f) 250 Ma Virgin Limestone Member (Moenkopi Formation, Nevada, USA). (a) Optical light image and (b, c) element maps ( $\mu$ XRF) of the stromatolite from the Woolly Dolomite. The  $\mu$ XRF maps were collected with a step size of 25  $\mu$ m and dwell time per pixel of 40 ms. The purple color in the element map indicates the combination of Ca and Mg (dolomite), while the distinct green domains indicate silica-rich components. The element maps illustrate the correlation with mineralogy, defining the alternating layers of chert

and carbonate. (d) Optical light image, and (e, f) element maps ( $\mu$ XRF) of the stromatolite from the Virgin Limestone. The  $\mu$ XRF maps were collected with a step size of 50  $\mu$ m and dwell time per pixel of 25 ms. The difference in element chemistry (represented by color differences compared with the Woolly Dolomite) indicate that the matrix to this rock is dominated by calcite, which has lower Mg and Fe content. Also, note the widely distributed, but thin bands of silica-rich rock.

Fig. 9. EBSD data for samples A1 and A2. The rose diagrams for the shape preferred orientations (SPO) of quartz and dolomite, which match the diagonal foliation seen in the outcrop and hand samples (e.g., **Fig 6**).

Fig. 10. Cartoon model for the formation of the *site A*  $\nabla$ -structures during deformation. (a) Block model showing the rock prior to deformation. (b) The same block showing the penetrative nature of the ridge-shaped  $\nabla$ -structures post-deformation. (b) Schematic block diagram illustrating post-deformation geometry of  $\nabla$ -structures (boudins) relative to the dominant stress axes ( $\sigma_1$ ,  $\sigma_2$ , and  $\sigma_3$ ) during the D<sub>1</sub>, D<sub>2</sub>, or both events. (d) Inferred process to generate the observed asymmetry of the  $\nabla$ -structures during the D<sub>2</sub> folding event. Flexural flow at amphibolite facies conditions on the limbs of folds would lead to asymmetry in  $\nabla$ -structures. Figure modified from Fossen (2016).

## SUPPLEMENTARY ONLINE INFORMATION

SUPPLEMENTARY FIGURES (Note, All Supplemental figures should be sized as 2-column fitting images)

SF1. Relative element intensity maps (relative X-ray counts measured by  $\mu$ XRF) of sample A1. Scale bar is 1 cm. Also provided is a false-color mineral distribution map of the sample produced by M4 TORNADO<sup>AMICS</sup> (Automated Mineral Identification and Characterization System) based on the same energy dispersive X-ray data used to generate element intensity maps.

SF2. Relative element intensity maps (relative X-ray counts measured by  $\mu$ XRF) of sample A2. Scale bar is 1 cm. Also provided is a false-color mineral distribution map of the sample produced by M4 TORNADO<sup>AMICS</sup>.

SF3. Polished hand sample and relative element intensity maps (relative X-ray counts measured by  $\mu$ XRF) of the Woolly Dolomite stromatolite sample. Scale bar is 1 cm. Also provided is a false-color mineral distribution map of the sample produced by M4 TORNADO<sup>AMICS</sup>.

SF4. Weathered surface, polished cut surface, and relative element intensity maps (relative X-ray counts measured by  $\mu$ XRF) of the stromatolite hand sample from the Virgin Limestone Member (Moenkopi Formation). Scale bar is 1 cm.

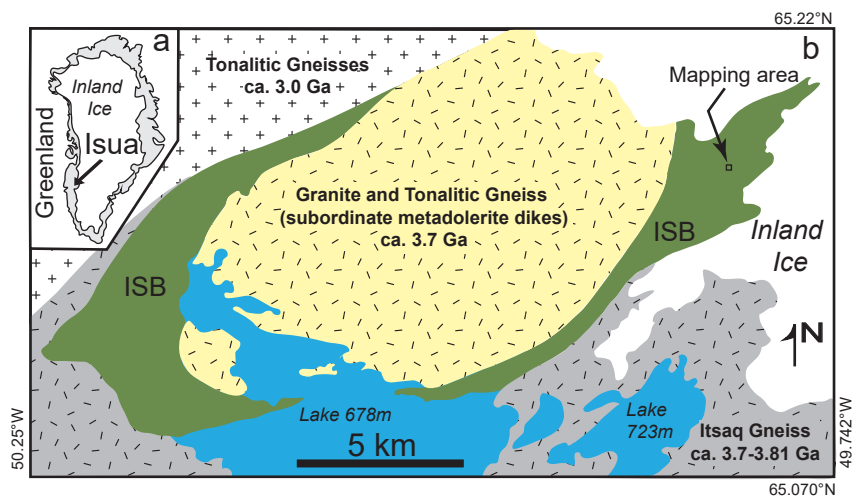
SF5. (a) Outcrop photograph of Site B (after Nutman et al., 2016) containing a single layer of pinch and swell structures (resembling mullions) that have not achieved full separation towards the  $\nabla$ -structure shape. Upper scale bar markings are in cm. A pygmatic dike that has cut the outcrop has a calculated length reduction of about two. (b) A sample from *site B* composed of layered quartz-rich rock (pale) and dolomitic calc-silicate schist (brown). White arrows indicate the positions of pinch structures formed during stretching of the layer to form ridges. Evidence for the ridge geometry can be seen in detail on the prominently weathered top edges of the quartz-rich layers. These ridges are parallel to lineations measured throughout the map area (**Fig. 4**). (c) Inset from (a) illustrating a quartz-rich layer with pinch and swell structures (white arrows) formed during deformation. (d) Photograph of sample B1a (cut face is parallel to the outcrop face, perpendicular to the orientation of ridge axes) from the larger sample in (b). Included are relative element intensity maps (relative X-ray counts measured by  $\mu$ XRF) illustrating the composition of laminated dolomitic calc-silicate schist. Images are presented as element concentration overlays where pink and orange colors (Ca + Fe and Ca + Mg, respectively) represent ferroan dolomite, green (Si) represents quartz. The dotted line represents the edge of the sample. (e) Photograph of sample B1b (cut face is perpendicular to the outcrop face, parallel to the orientation of ridge axes) from the larger sample in (b). The contacts between the quartz and carbonate layers is nearly planar (in 3D). Images are presented as element concentration overlays where pink and orange colors (Ca + Fe and Ca + Mg, respectively) represent ferroan dolomite, green (Si) represents quartz.  $\mu$ XRF maps for both samples were collected using X-ray source conditions of 50 kV and 600  $\mu$ A, a step size of 50  $\mu$ m and dwell time per pixel of 35 ms.

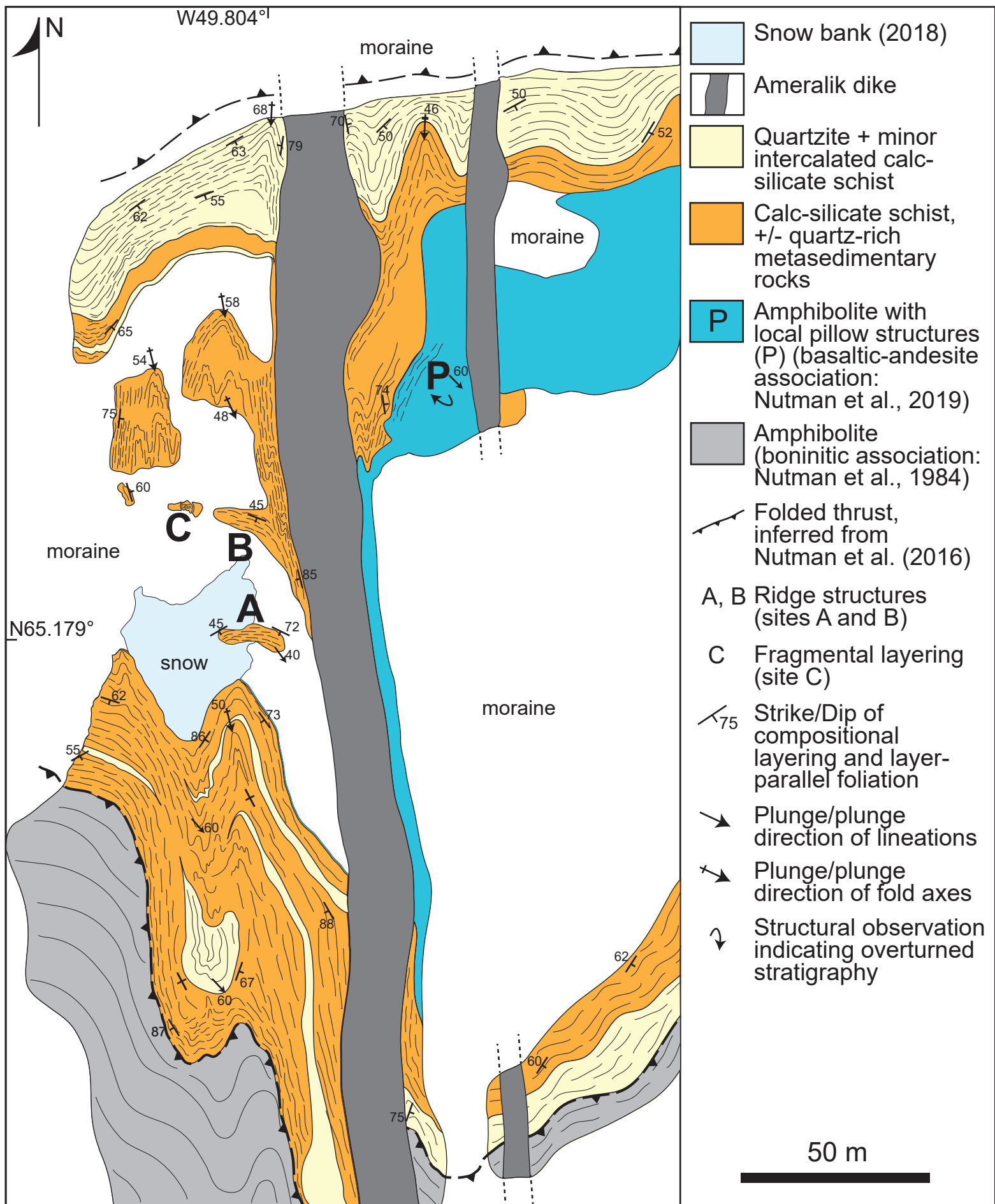
SF6. Relative element intensity maps (relative X-ray counts measured by  $\mu$ XRF) of sample B1a from Site B (see **Supplementary Figure 5** for sample orientation). Scale bar is 1 cm.

SF7. Relative element intensity maps (relative X-ray counts measured by  $\mu$ XRF) of sample B1b from Site B (see **Supplementary Figure 5** for sample orientation). Scale bar is 1 cm.

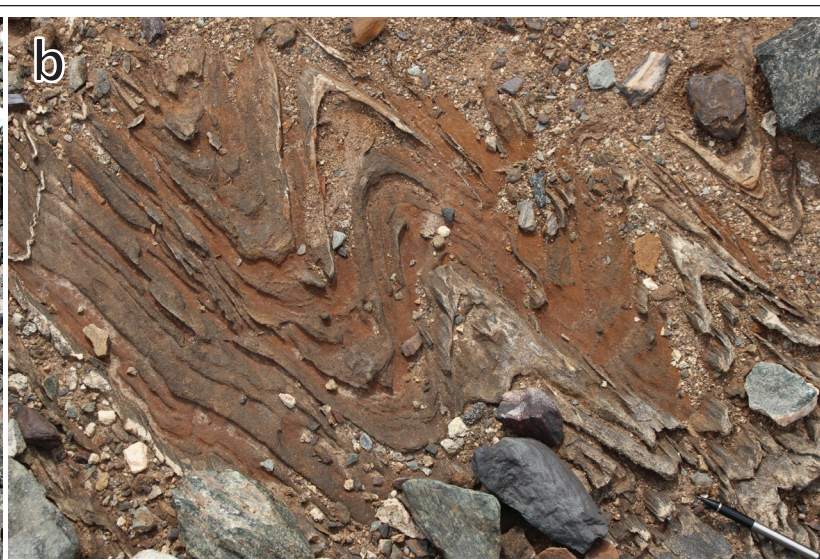
SF8. EBSD data for the two samples for surfaces cut parallel and perpendicular to the ridge shaped  $\nabla$ -structures. (a) Structural orientation of surface analyzed by EBSD on Sample A1, parallel to  $\nabla$ -structure. (b) Map and table of EBSD data color-coded by mineral solution to diffraction patterns. (c) Rose diagrams of long-axis orientations of quartz and dolomite grains showing little SPO. (d) Pole figures and misorientation distribution functions for dolomite. Pole figures show poles to the (a) and (c) planes with low multiples of uniform distribution (MUD). Misorientation distribution functions for neighboring pairs show a peak ca.  $160^\circ$  but non-neighboring grains show a near-random distribution. (e) Pole figures and misorientation distribution functions for quartz. Pole figures show poles to the (a) and (c) planes with low multiples of uniform distribution (MUD). Misorientation distribution functions for neighboring pairs show a peak ca.  $20^\circ$  but non-neighboring grains show a near-random distribution. (f) Structural orientation of surface analyzed by EBSD on Sample A1, perpendicular to  $\nabla$ -structure. (g) Map and table of EBSD data color-coded by mineral solution to diffraction patterns. (h) Rose diagrams of long-axis orientations of quartz and dolomite grains showing a SPO within the plane of S2. (i) Pole figures and misorientation distribution functions for dolomite. Pole figures show poles to the (a) and (c) planes with low multiples of uniform distribution (MUD). Misorientation distribution functions for neighboring pairs show a peak ca.  $160^\circ$  but non-neighboring grains show a near-random distribution. (j) Pole figures and misorientation distribution functions for quartz. Pole figures show poles to the (a) and (c) planes with low multiples of uniform distribution (MUD). Misorientation distribution functions for neighboring pairs show a peak ca.  $20^\circ$  but non-neighboring grains show a near-random distribution. (k) Structural orientation of surface analyzed by EBSD on Sample A2, parallel to  $\nabla$ -structure. (l) Map and table of EBSD data color-coded by mineral solution to diffraction patterns. (m) Rose diagrams of long-axis orientations of quartz and dolomite grains showing a moderate SPO. (n) Pole figures and misorientation distribution functions for dolomite. Pole figures show poles to the (a) and (c) planes with low multiples of uniform distribution (MUD). (o) Pole figures and misorientation distribution functions for quartz. Pole figures show poles to the (a) and (c) planes with low multiples of uniform distribution (MUD). Misorientation distribution functions for neighboring pairs show a peak ca.  $20^\circ$  but non-neighboring grains show a near-random distribution. (p) Structural orientation of surface analyzed by EBSD on Sample A2, perpendicular to  $\nabla$ -structure. (q) Map and table of EBSD data color-coded by mineral solution to diffraction patterns. (r) Rose diagrams of long-axis orientations of quartz and dolomite grains showing an SPO in the plane of F2. (s) Pole figures and misorientation distribution functions for dolomite. Pole figures show poles to the (a) and (c) planes with low multiples of uniform distribution (MUD). Misorientation distribution functions for neighboring pairs show a peak ca.  $160^\circ$  but non-neighboring grains show a near-random distribution. (t) Pole figures and misorientation distribution functions for quartz. Pole figures show poles to the (a) and (c) planes with low multiples of uniform distribution (MUD). Misorientation distribution functions for neighboring pairs show a peak ca.  $20^\circ$  but non-neighboring grains show a near-random distribution.

Supplementary Table 1. Summary of EBSD-derived grain statistics used in **Figure 9**.

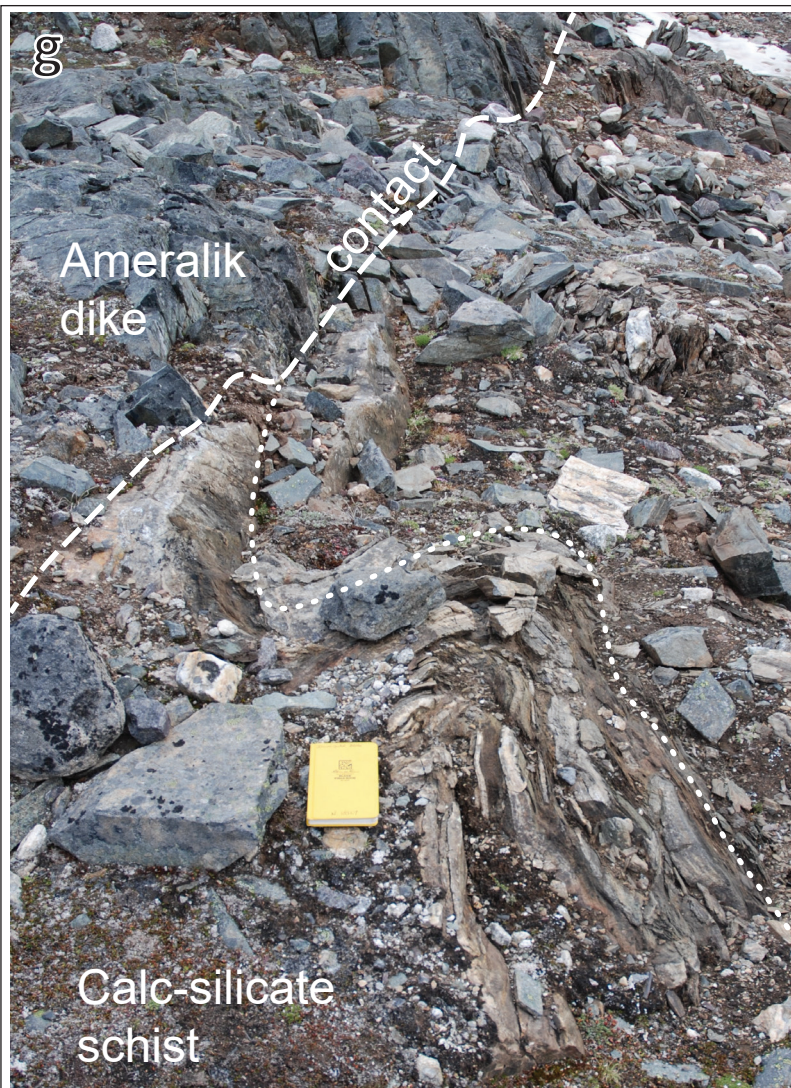


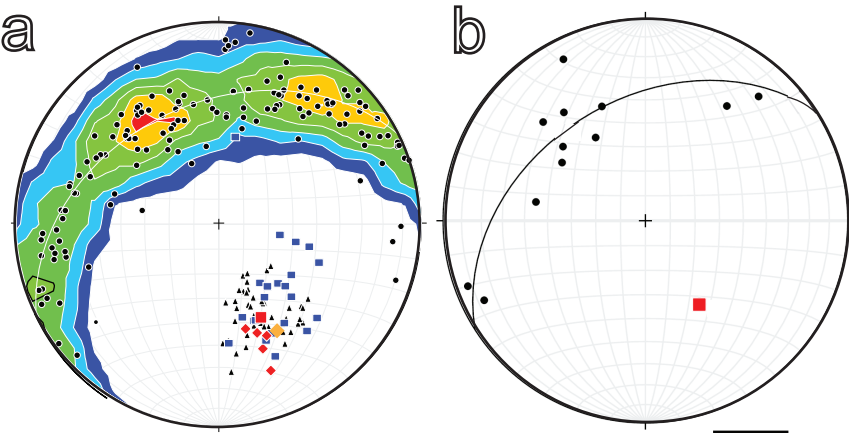






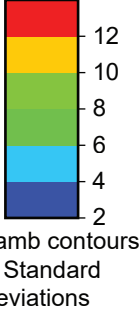






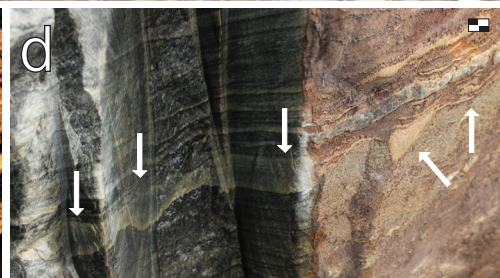
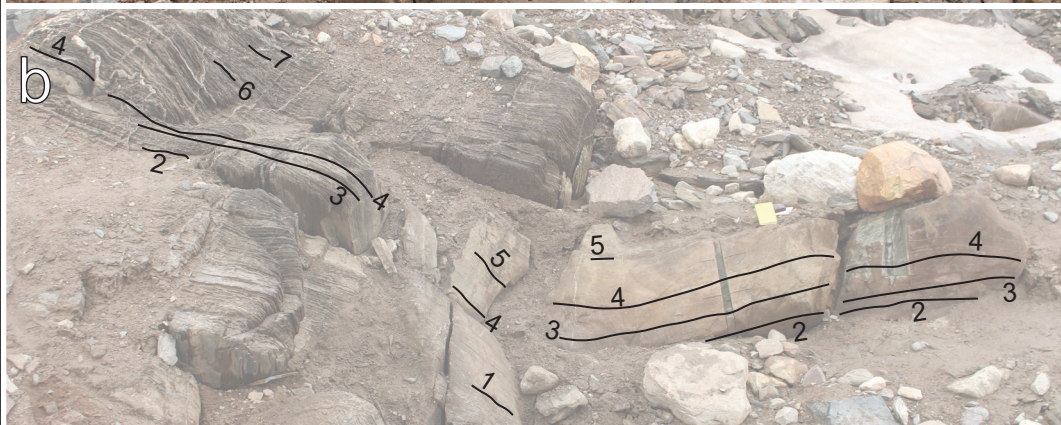
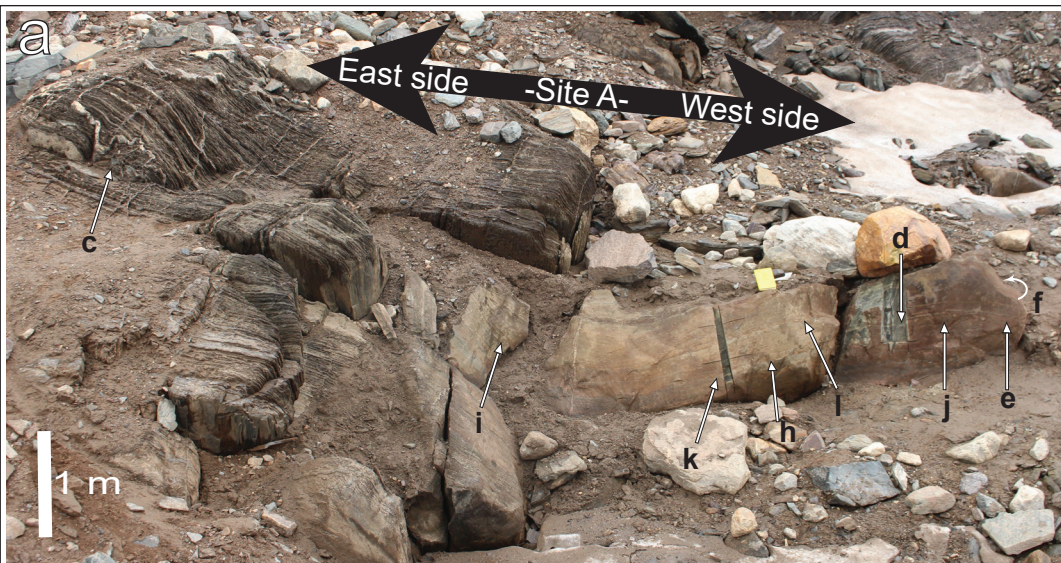
Key:

- Plunge and plunge direction of fold hinges
- ◆ Plunge and plunge direction of ridge-shaped  $\nabla$ -structures
- ◆ Estimated plunge and plunge direction of proposed stromatolite used in Nutman et al. (2016)
- ▲ Plunge and plunge direction of lineations
- Pole to planes of compositional layering
- Pi-axis

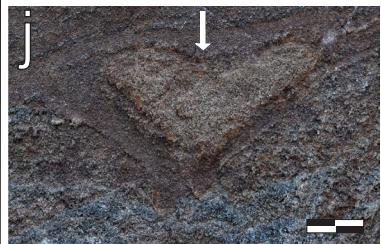
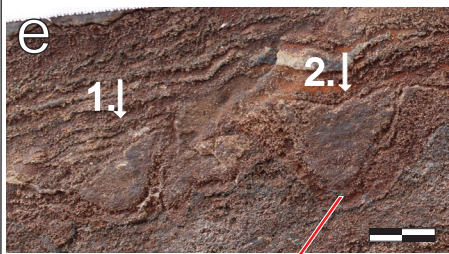


Kamb contours  
in Standard  
Deviations

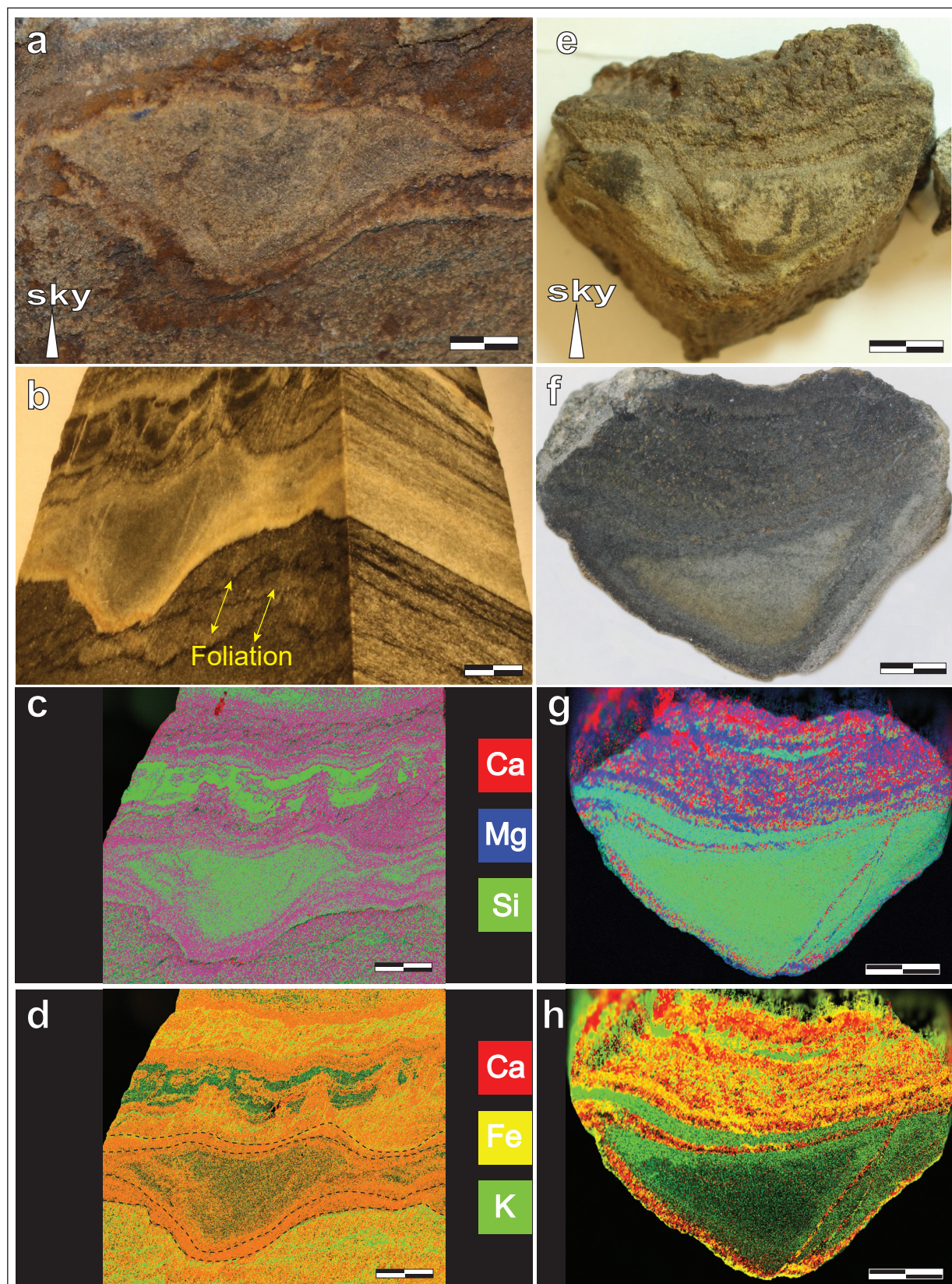




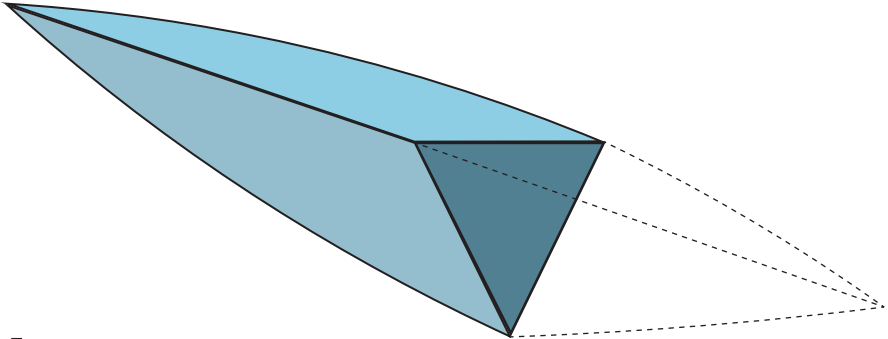




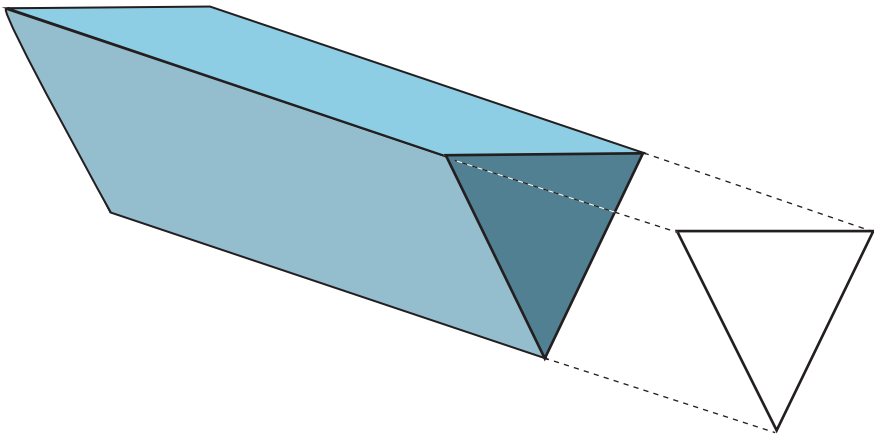




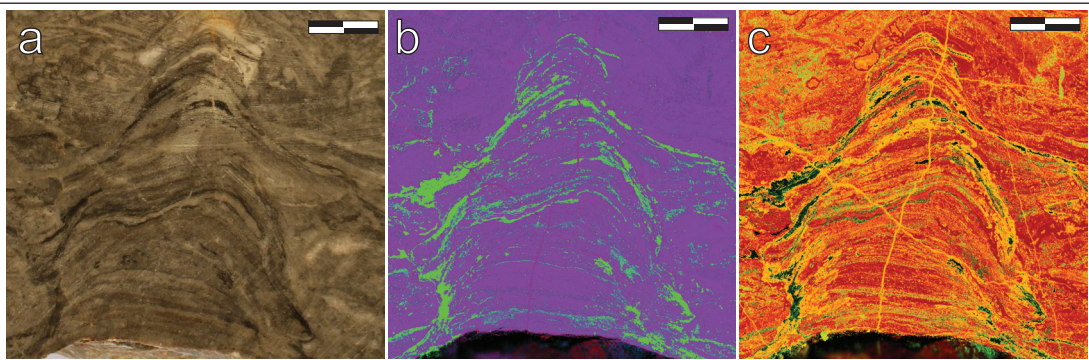
a



b







Ca

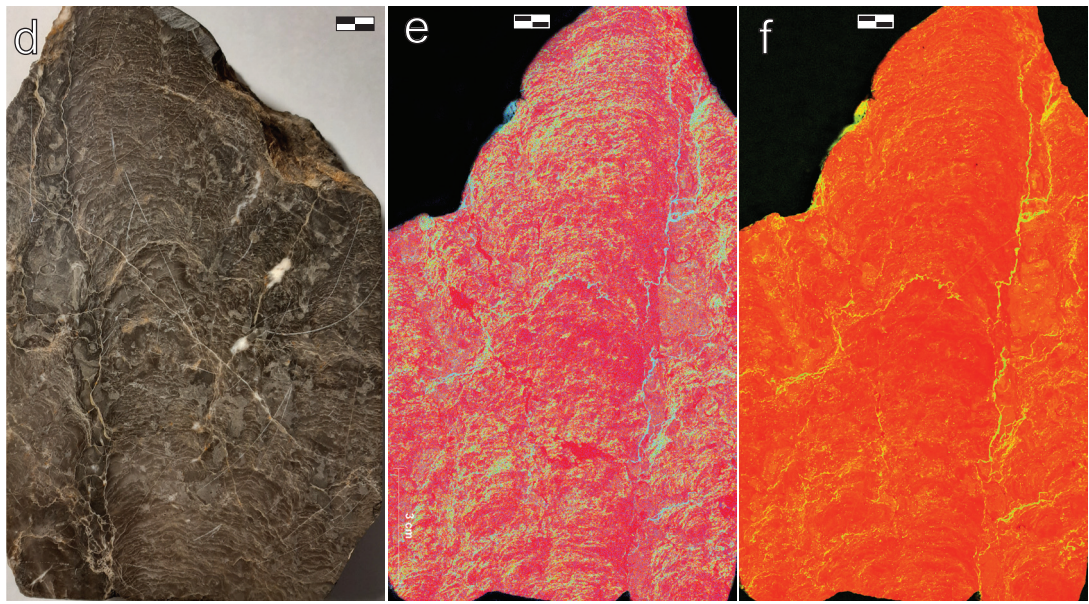
Mg

Si

Ca

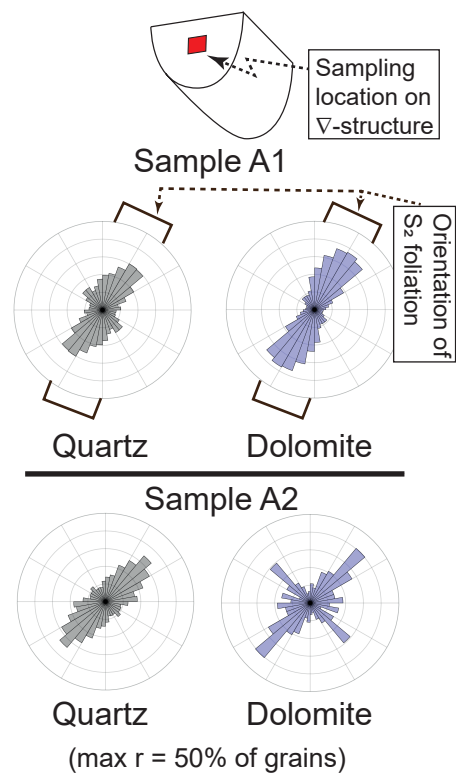
Fe

K

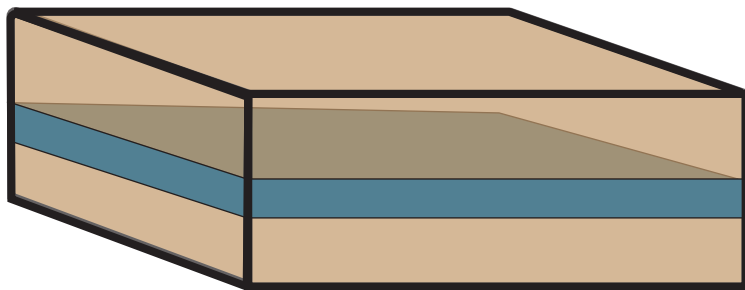




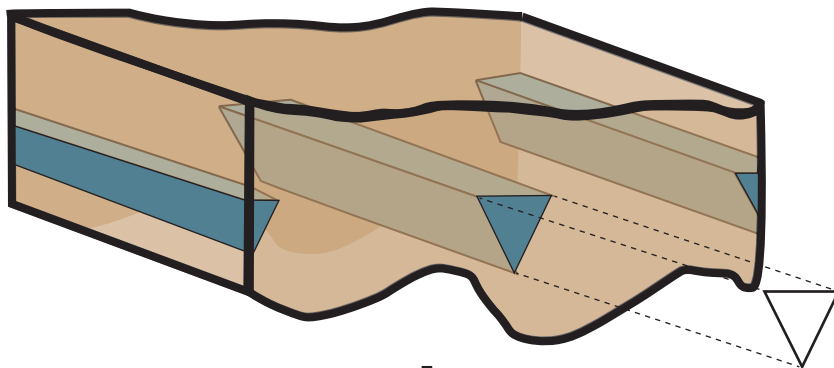
Grain long axis orientations (SPO)



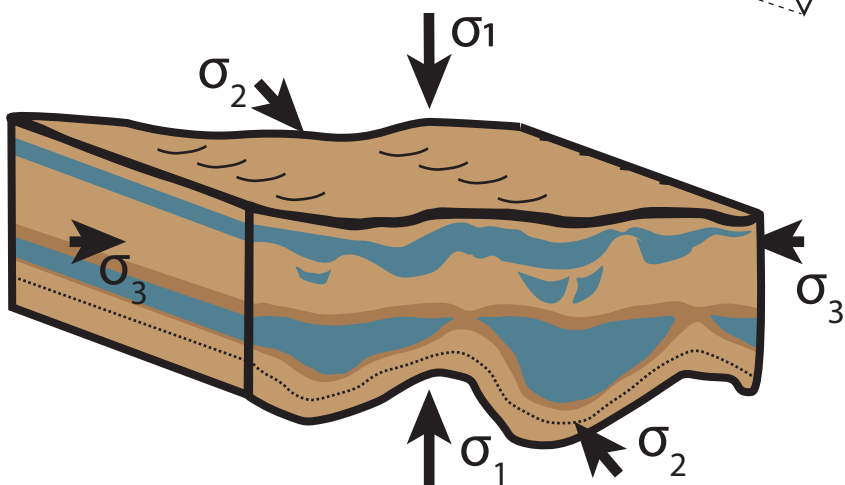
a



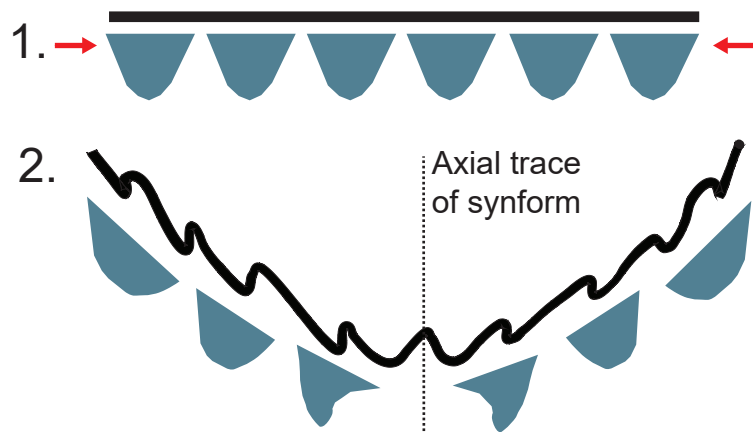
b



c

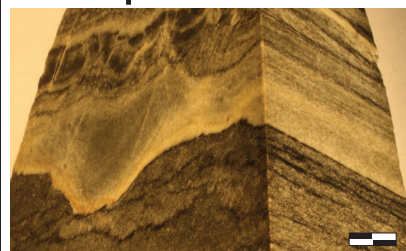


d

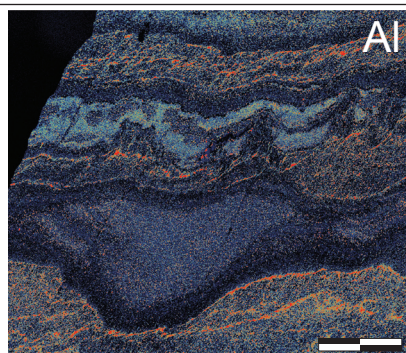




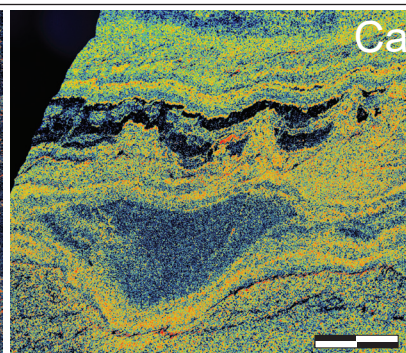
# Sample A1



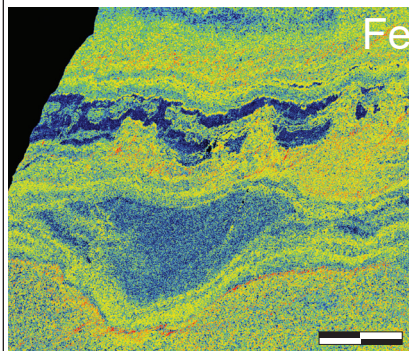
Hand sample



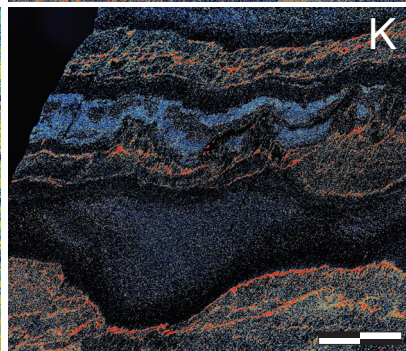
Al



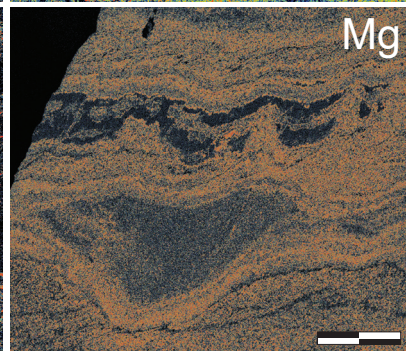
Ca



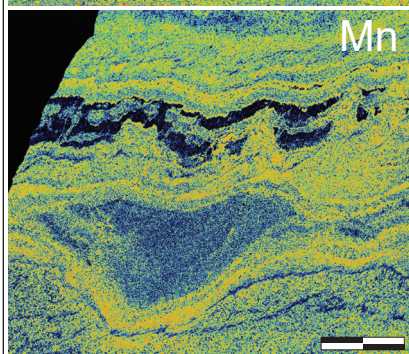
Fe



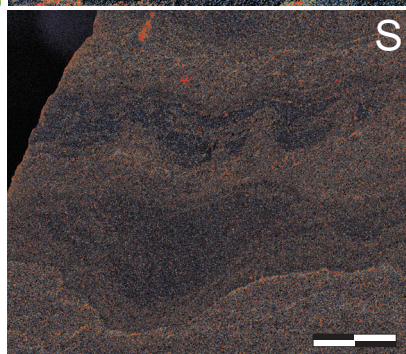
K



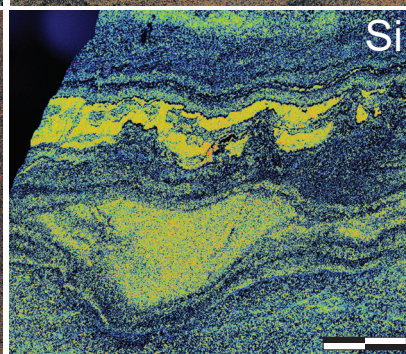
Mg



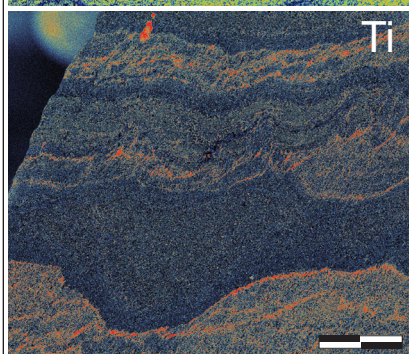
Mn



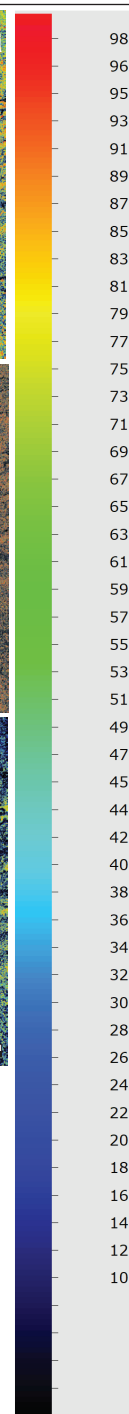
S



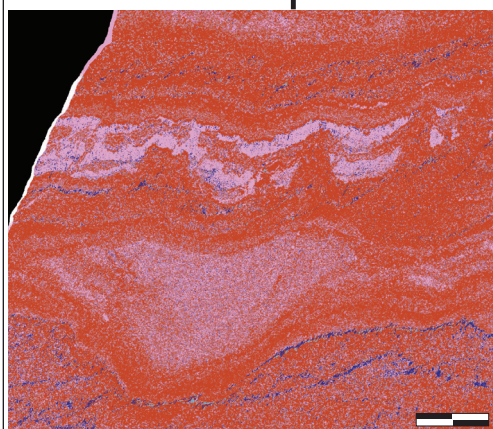
Si



Ti



## Mineral map

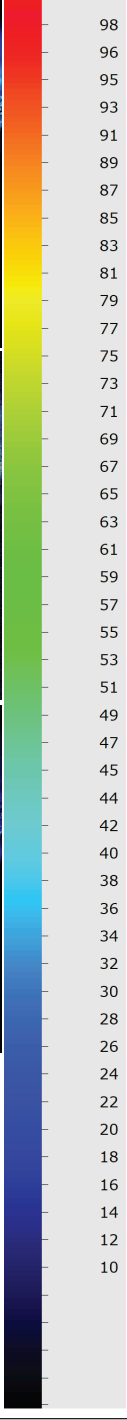
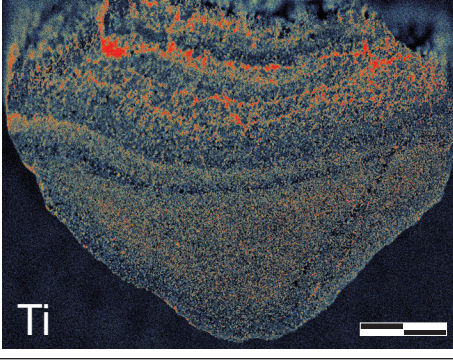
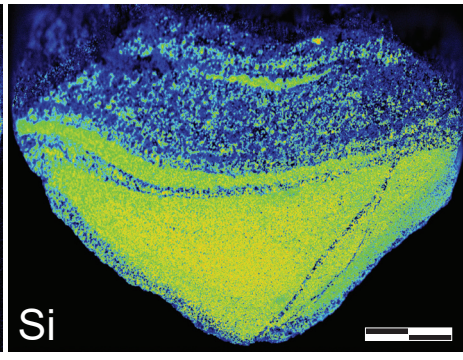
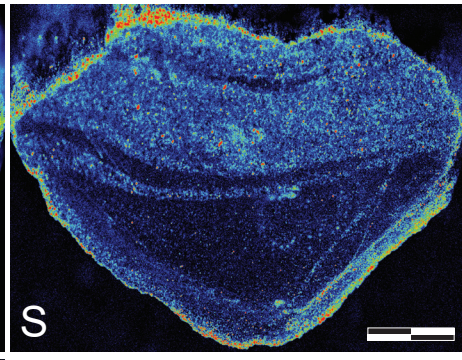
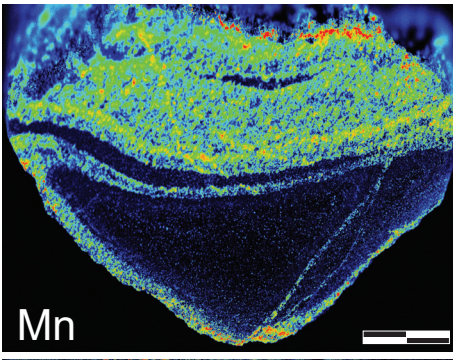
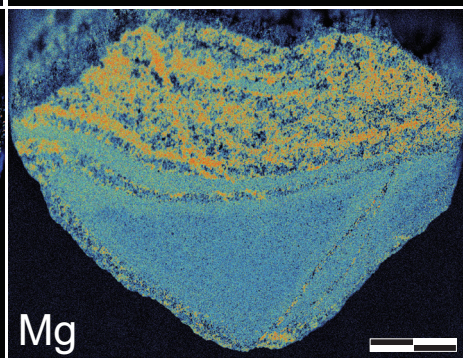
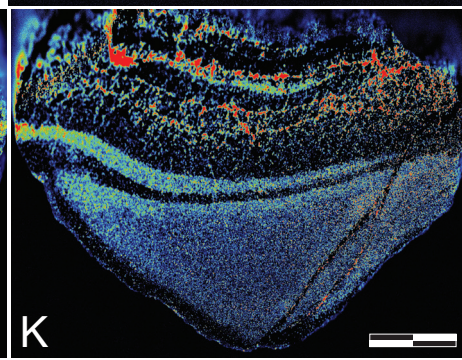
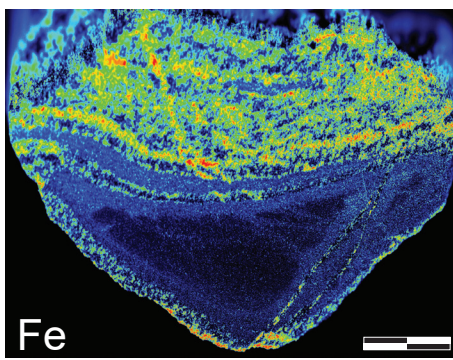
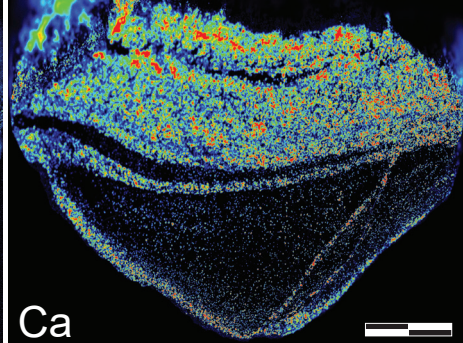
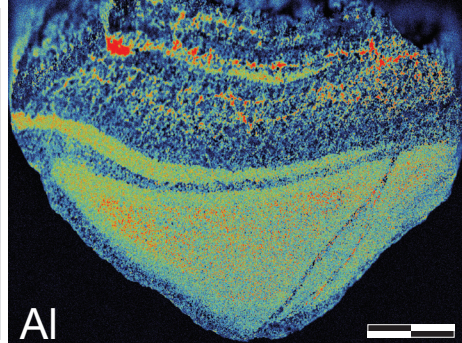
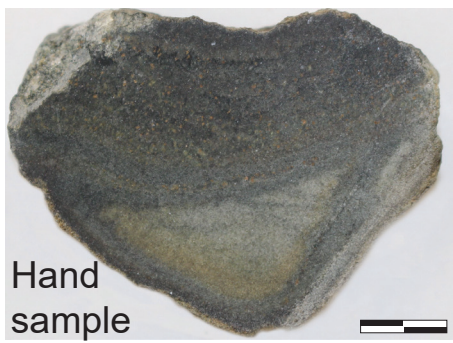


Key:

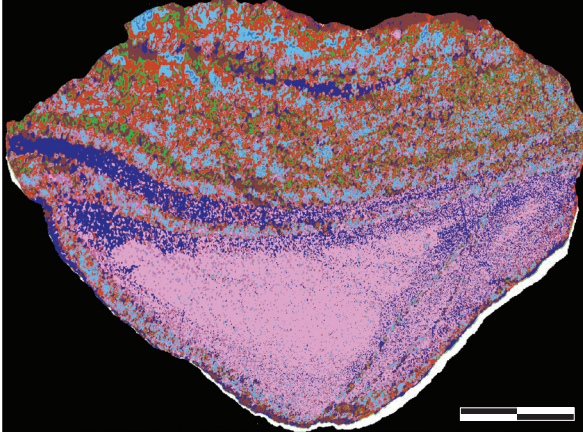
- Quartz
- Dolomite
- Ankerite
- Biotite
- Hematite



# Sample A2



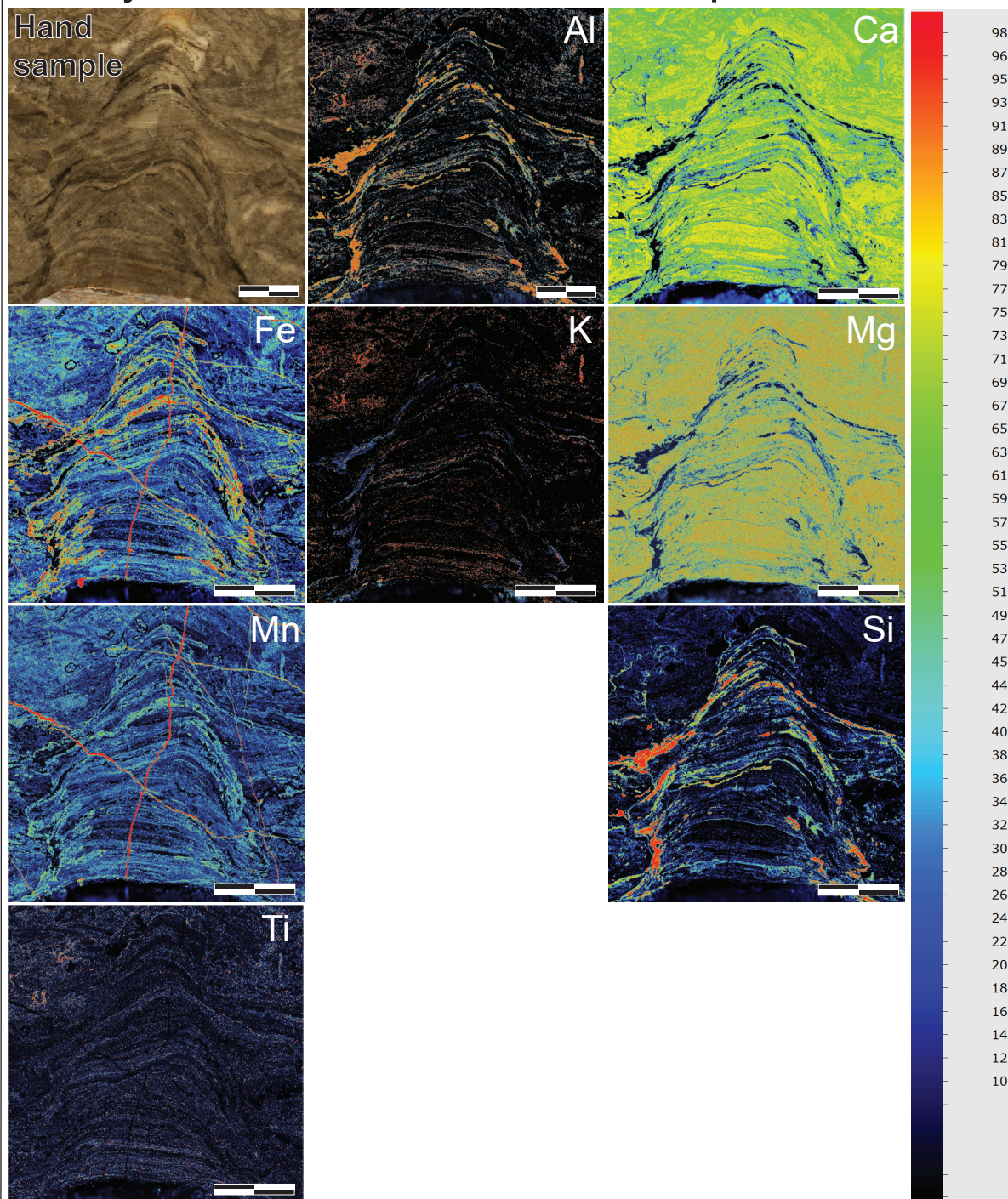
## Mineral map



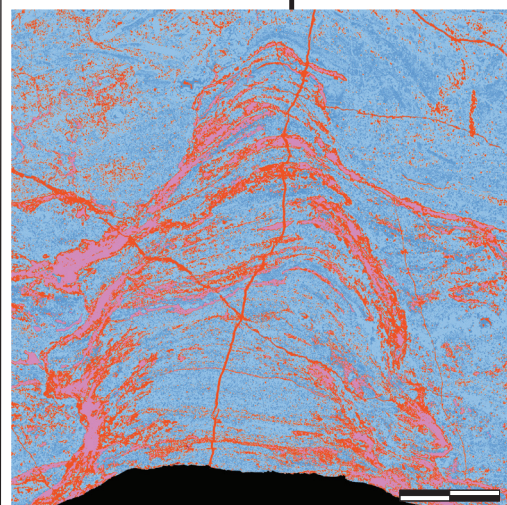
- Key
- Quartz
  - Dolomite
  - Ankerite
  - Biotite
  - Hematite
  - Actinolite



# Wooly Dolomite stromatolite sample



## Mineral map

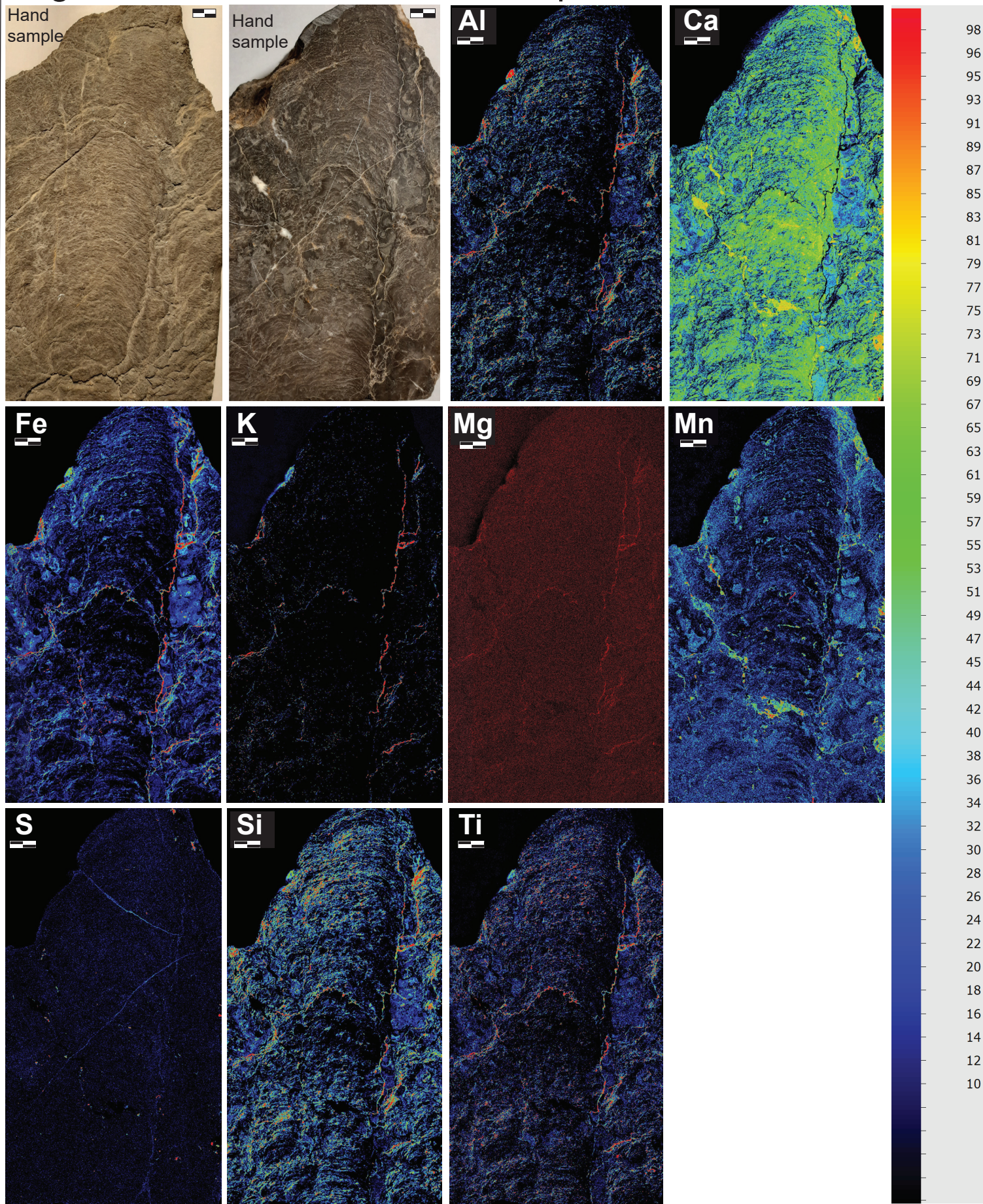


### Key

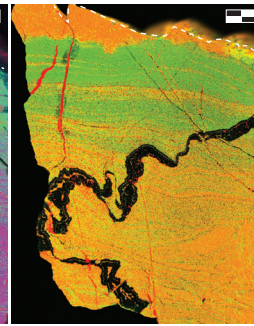
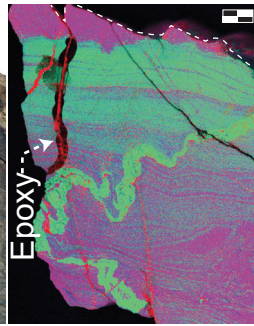
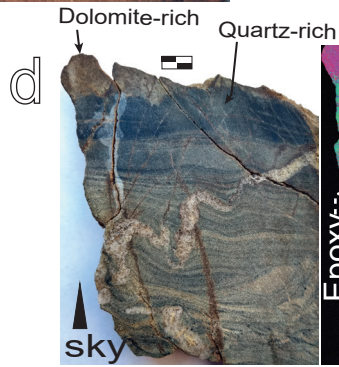
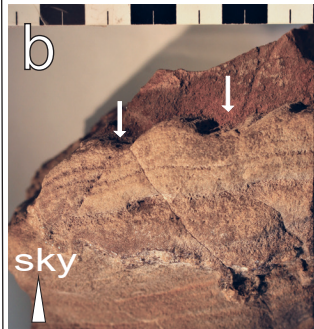
- Quartz
- Dolomite
- Ferroan Dolomite (mid)
- Ferroan Dolomite (high)



# Virgin Limestone stromatolite sample







Ca

Mg

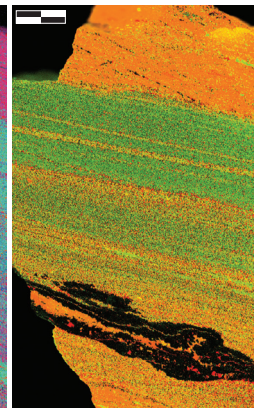
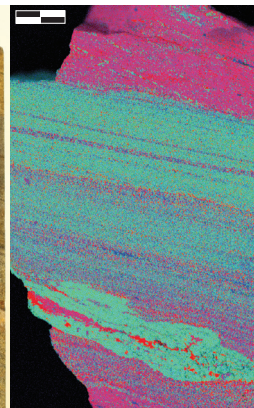
Si

Ca

Fe

K

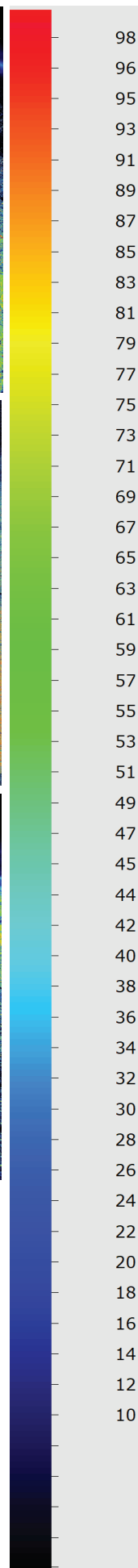
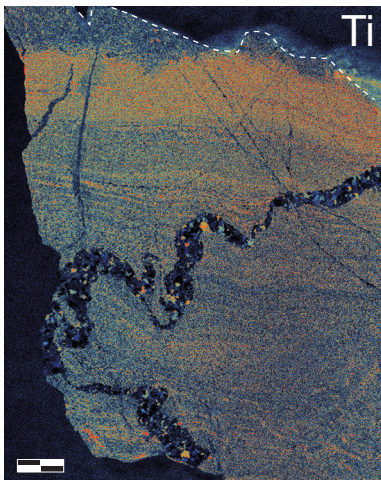
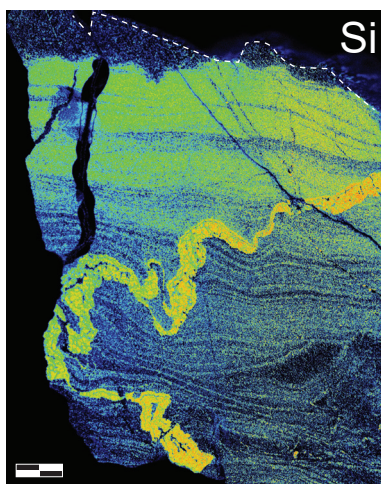
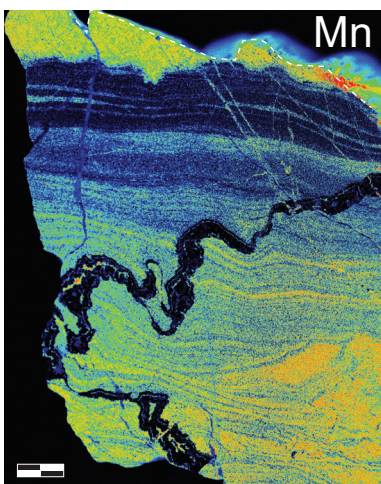
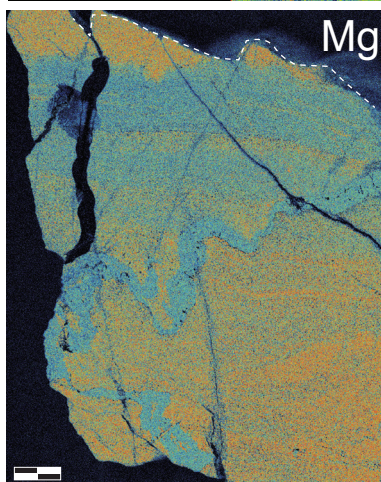
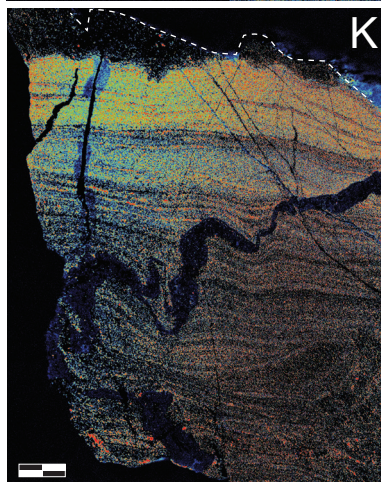
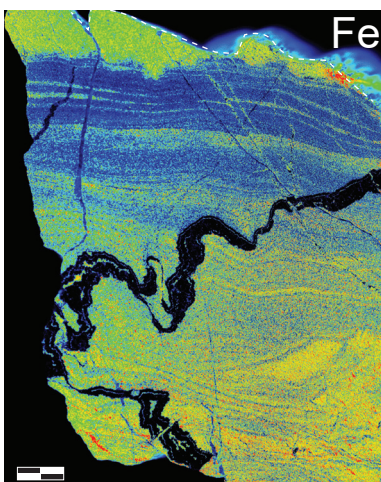
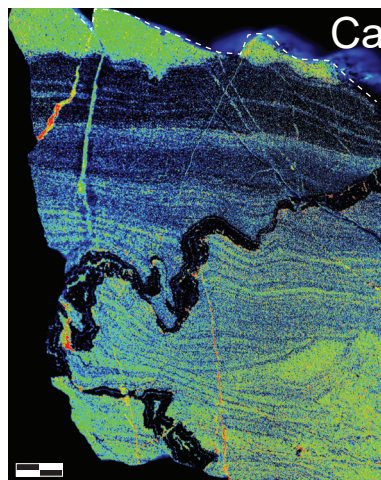
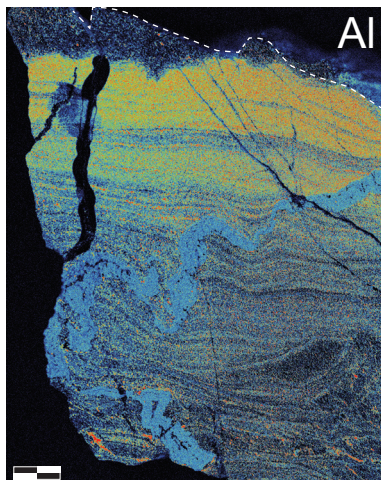
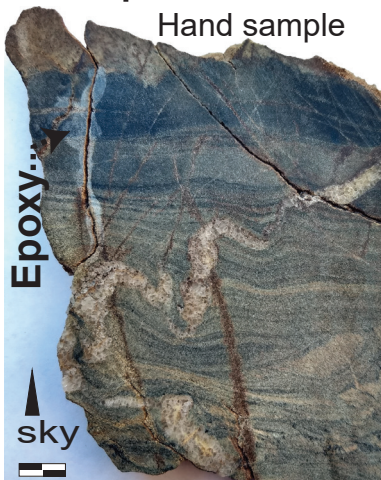
e





# Sample B1a

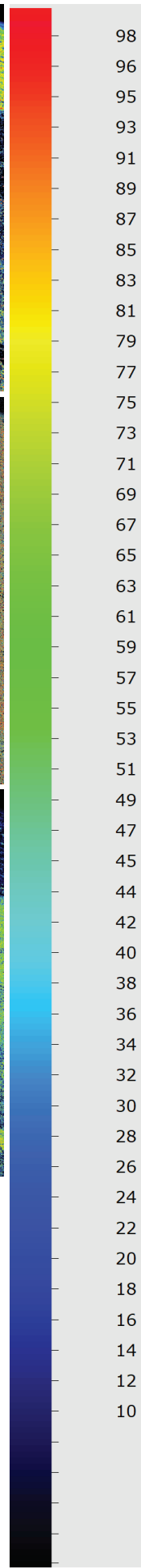
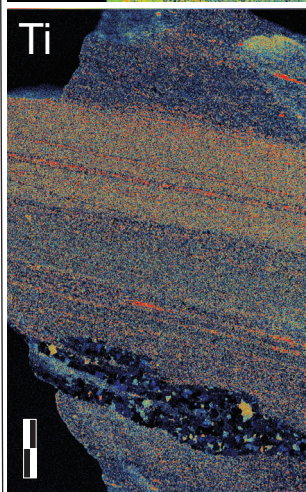
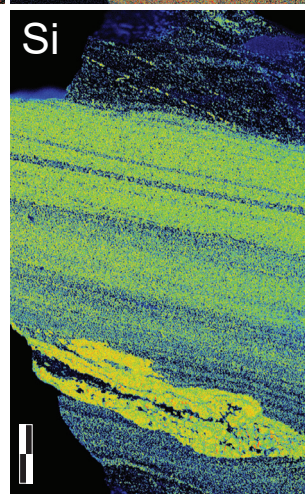
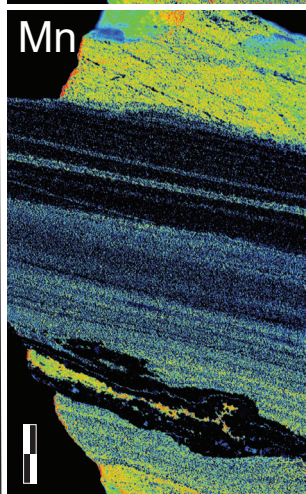
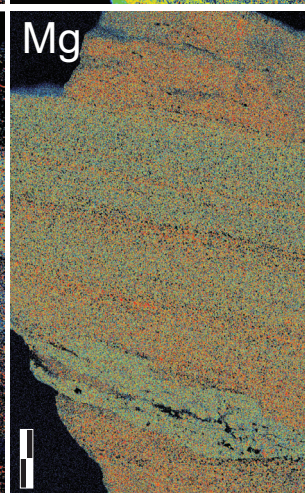
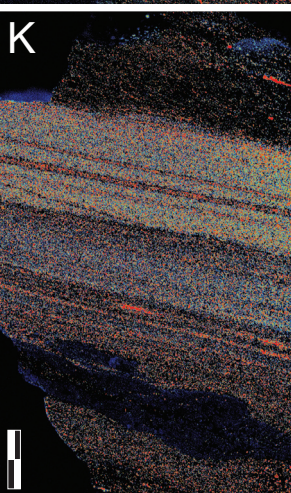
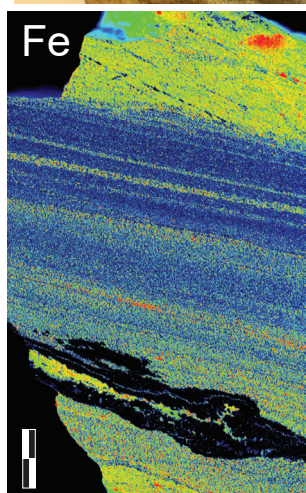
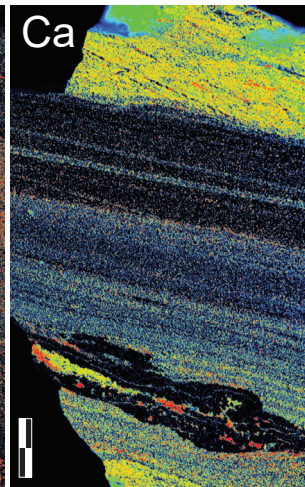
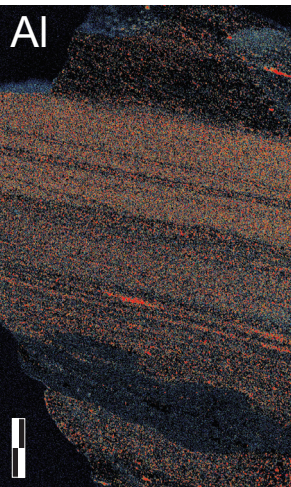
Hand sample





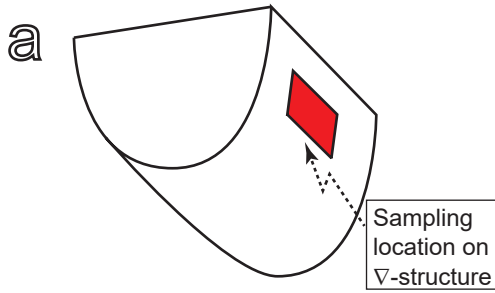
# Sample B1b

Hand sample



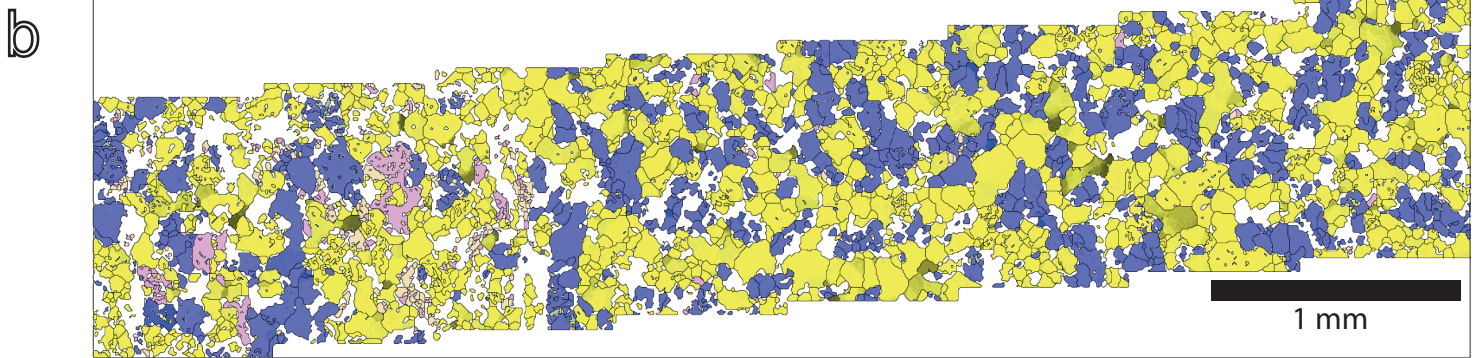


# Sample A1- Parallel to $\nabla$ -structures

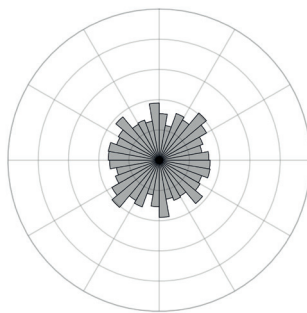


notIndexed
Quartz-new
Muscovite
Grossular
Clinozoisite
Jadeite
Orthoclase
Annite
Dolomite
Tremolite
Actinolite
Tourmaline

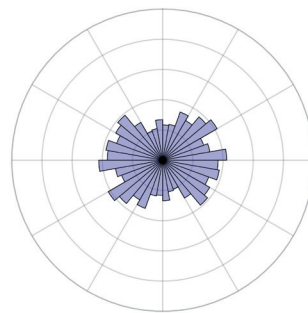
Grains	Pixels	Mineral
156	67906	notIndexed
1380	58910	Quartz-new
141	2195	Muscovite
8	28	Clinozoisite
4	13	Orthoclase
145	1366	Annite
814	29709	Dolomite
2	6	Tremolite
21	130	Tourmaline



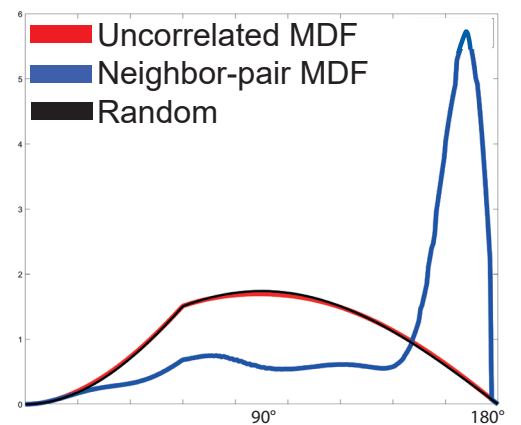
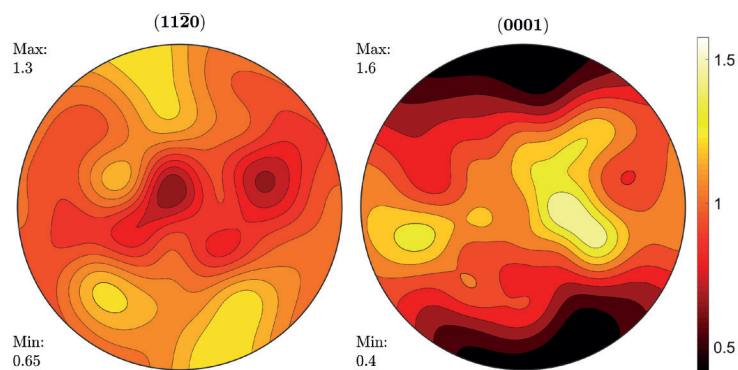
c Quartz grain long axis orientations (max r = 0.5)

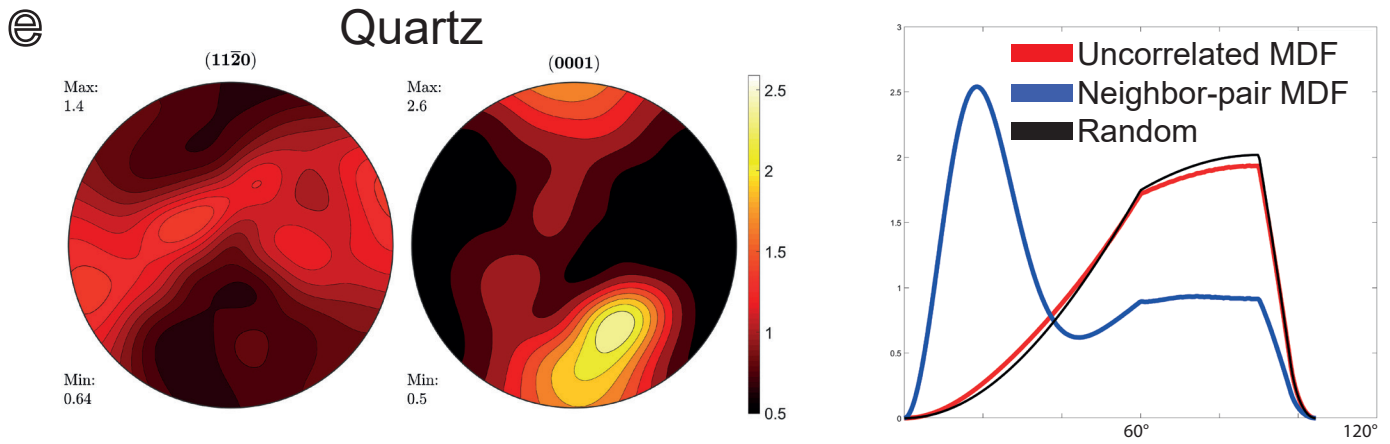


Dolomite grain long axis orientations (max r = 0.5)

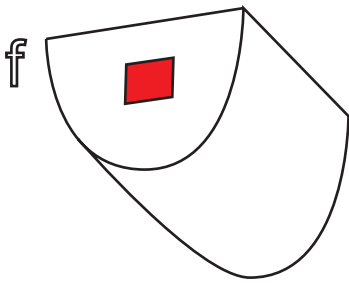


d Dolomite



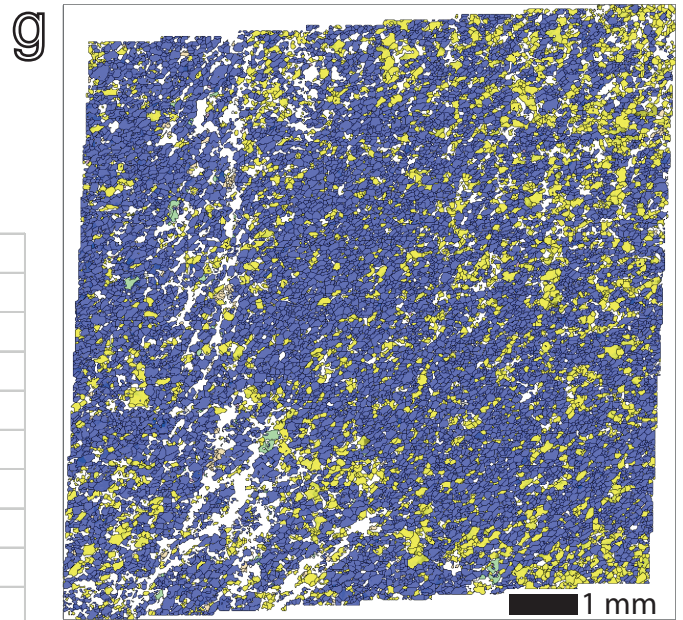


## Sample A1- Perpendicular to $\nabla$ -structures



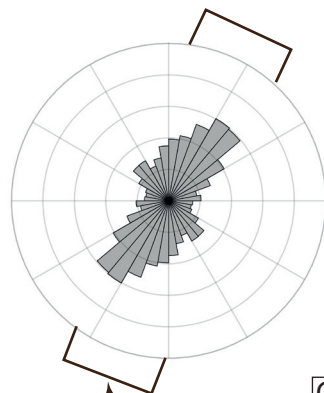
notIndexed
Quartz-new
Clinozoisite
Orthoclase
Annite
Dolomite
Tremolite
Actinolite
Tourmaline

Grains	Pixels	Mineral
192	51818	notIndexed
4103	52638	Quartz-new
34	185	Clinozoisite
23	106	Orthoclase
186	1161	Annite
11965	176405	Dolomite
9	35	Tremolite
6	21	Actinolite
46	810	Tourmaline

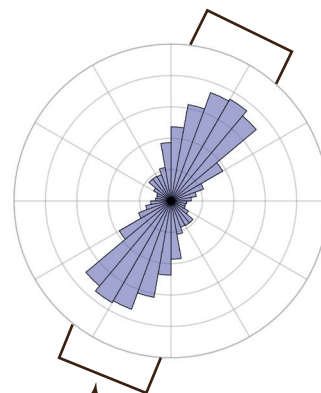


h

Quartz grain long axis  
orientations (max r = 0.5)



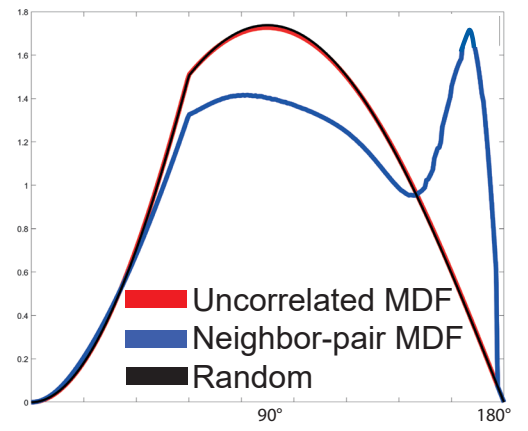
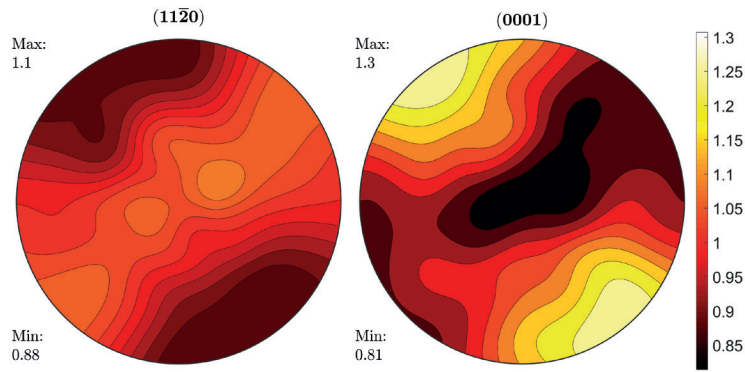
Dolomite grain long axis  
orientations (max r = 0.5)



Orientation of  
 $S_2$  foliation

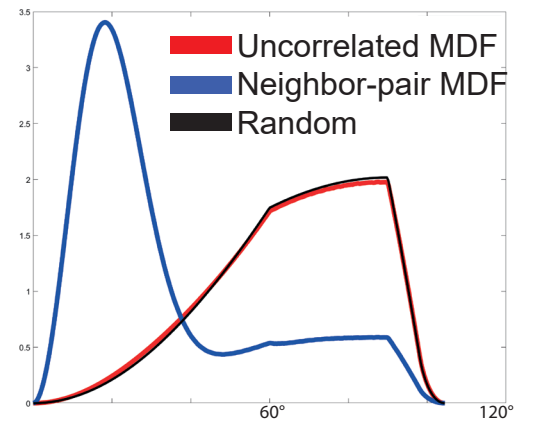
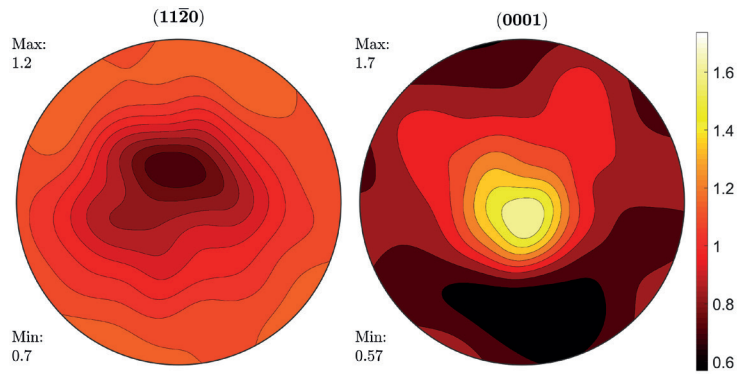
# Dolomite

i

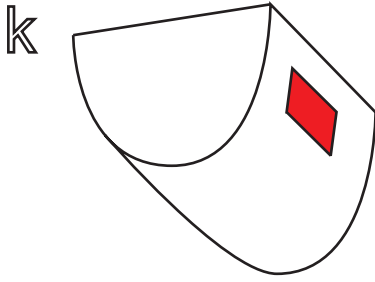


# Quartz

j

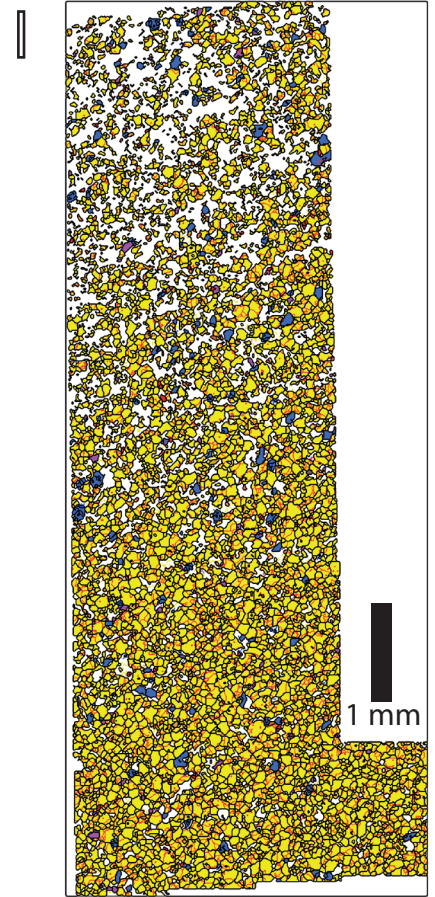


# Sample A2- Parallel to $\nabla$ -structures



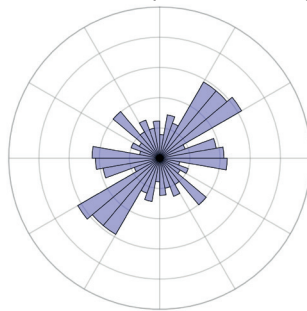
	notIndexed
	Quartz-new
	Muscovite
	Orthoclase
	Annite
	Dolomite
	Phlogopite

Grains	Pixels	Mineral
117	61845	notIndexed
4862	73526	Quartz-new
95	611	Muscovite
6	20	Orthoclase
94	509	Annite
257	2644	Dolomite
61	275	Phlogopite

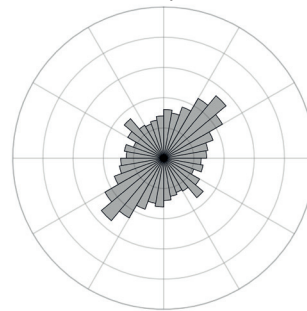


m

Dolomite grain long axis  
orientations (max r = 0.5)

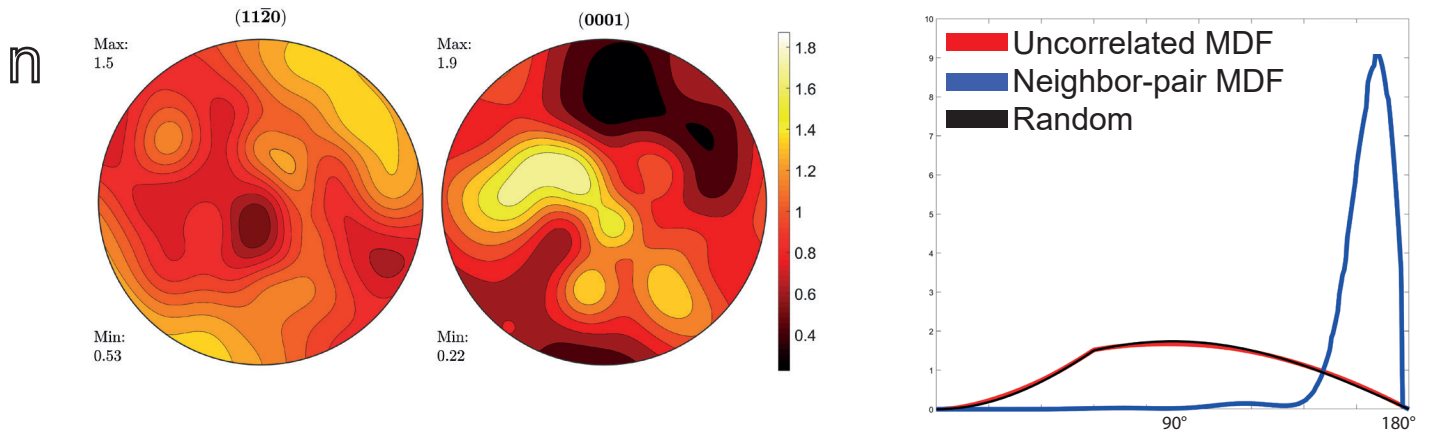


Quartz grain long axis  
orientations (max r = 0.5)

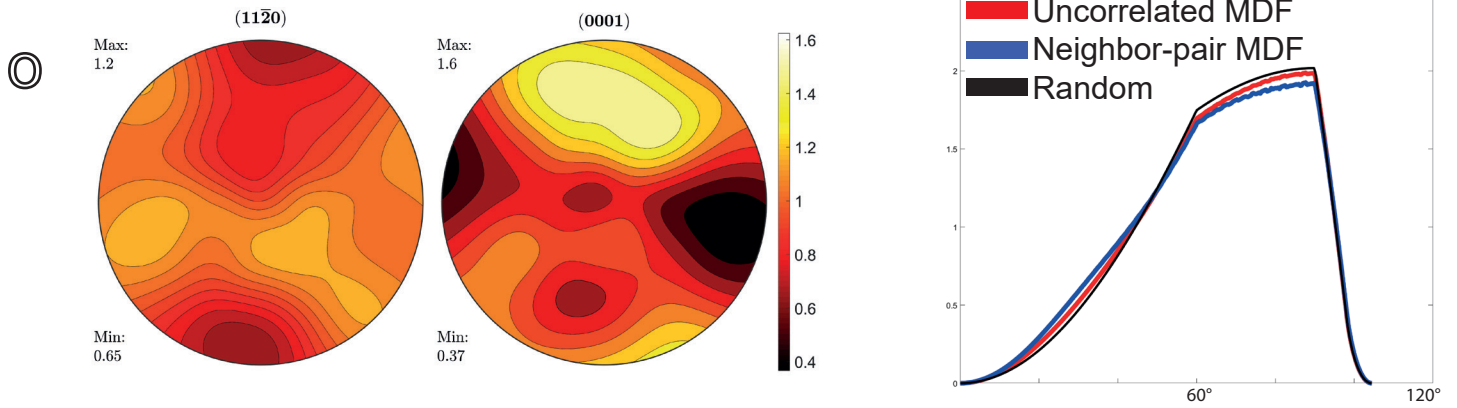




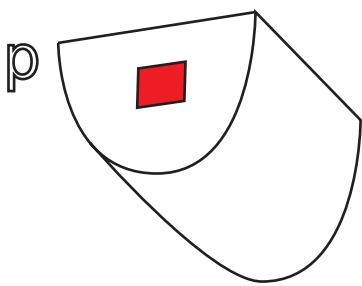
## Dolomite



## Quartz



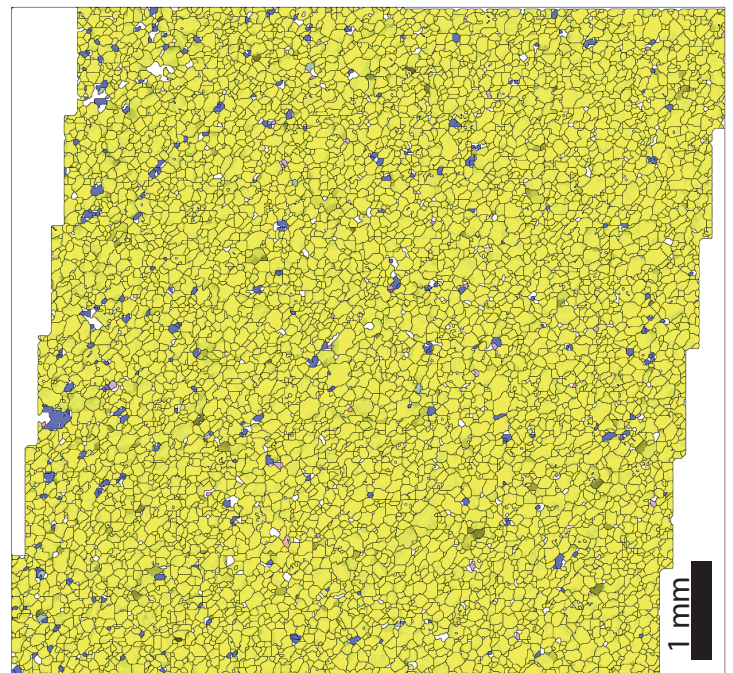
## Sample A2- Perpendicular to $\nabla$ -structures



**q**

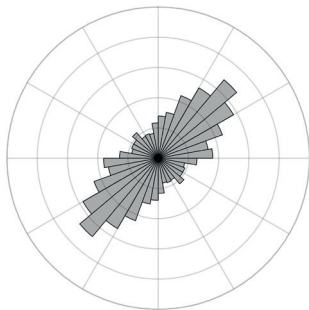
notIndexed
Quartz-new
Muscovite
Clinozoisite
Orthoclase
Annite
Dolomite
Phlogopite
Tourmaline

Grains	Pixels	Mineral
8	12562	notIndexed
6374	117827	Quartz-new
21	117	Muscovite
1	5	Clinozoisite
8	37	Orthoclase
1	3	Annite
263	1833	Dolomite
6	36	Phlogopite
16	105	Tourmaline

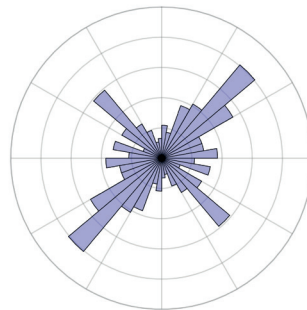


r

Quartz grain long axis  
orientations (max r = 0.5)

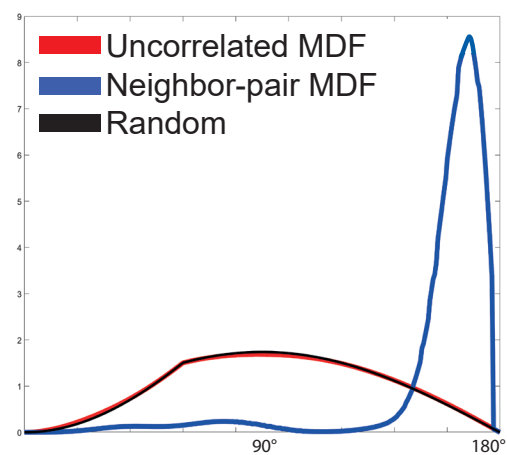
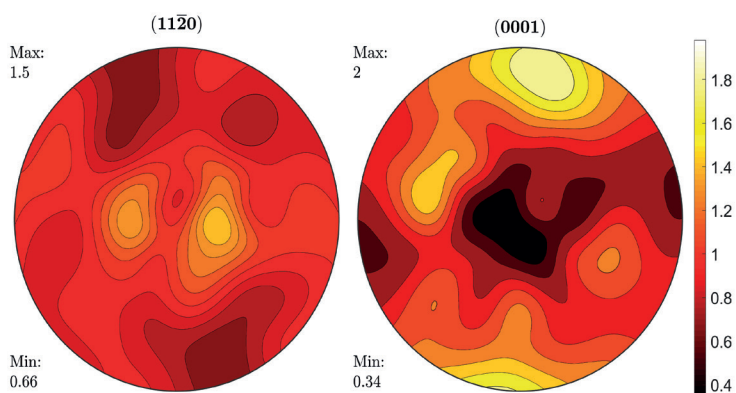


Dolomite grain long axis  
orientations (max r = 0.5)



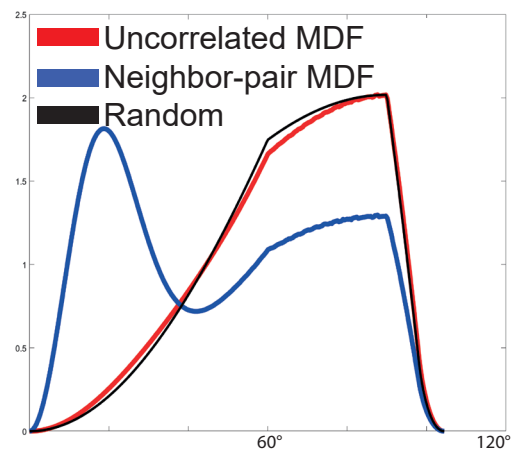
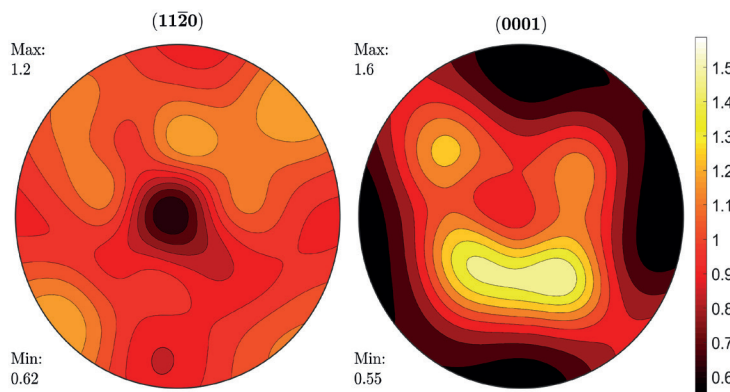
## Dolomite

S



t

## Quartz



Supplemental Table 1.

Sample location	Sample orientation	Mineral	Measurements/ pixels	Grains	Mean GOS (°)	M-index	Mean aspect ratio	Log-normal mean grain size (µm)	Grain size 2- sigma upper (µm)	Grain size 2- sigma lower (µm)
A1	Parallel	Quartz	52,638	4,103	0.7684	0.0118	1.49	45.5	108.4	19.1
		Dolomite	176,405	11,965	0.4496	0.0025	1.54	50.2	116.5	21.6
	Perpendicular	Quartz	58,910	1,380	0.6864	0.0221	1.51	32.3	121.8	8.6
		Dolomite	29,709	814	0.5538	0.0099	1.55	30.3	108.1	8.5
A2	Parallel	Quartz	73,526	4,862	0.7264	0.0161	1.44	55.4	136.5	22.5
		Dolomite	2,644	257	0.3338	0.0159	1.48	46.5	104.4	20.7
	Perpendicular	Quartz	117,827	6,374	0.8607	0.0172	1.45	63.0	151.5	26.2
		Dolomite	1,833	263	0.3782	0.0112	1.47	40.6	77.2	21.4